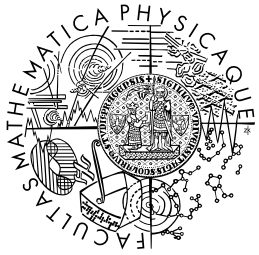

FACULTY
OF MATHEMATICS
AND PHYSICS
Charles University

MASTER THESIS

Ondřej Novák

FDTD simulations of functional photonic structures

Institute of Physics of Charles University

Supervisor of the master thesis: RNDr. Martin Veis, Ph.D.
Study programme: Physics
Study branch: Optics and optielectronics

Prague 2021

I declare that I carried out this master thesis independently, and only with the cited sources, literature and other professional sources. It has not been used to obtain another or the same degree.

I understand that my work relates to the rights and obligations under the Act No. 121/2000 Sb., the Copyright Act, as amended, in particular the fact that the Charles University has the right to conclude a license agreement on the use of this work as a school work pursuant to Section 60 subsection 1 of the Copyright Act.

In ..... date ....

Author's signature

Dedication.

Title: FDTD simulations of functional photonic structures

Author: Ondřej Novák

institute: Institute of Physics of Charles University

Supervisor: RNDr. Martin Veis, Ph.D., Institute of Physics of Charles University

Abstract: This thesis aims to (i) design and optimize the geometry of magneto-photonic crystal based on ferromagnetic garnet in order to resonantly enhance the magneto-optical response, (ii) to explore the possibility of using magnetic shape memory alloy to build an optically active photonic element, using advanced FDTD modeling. A Faraday rotation of 180° was reached but with low values of transmissivity. An investigation of the origin of such high values of Faraday rotation led to a conclusion that such structure has to be highly sensitive towards a change of a refractive index of its surroundings. This was confirmed, and so further development of this structure can lead to an efficient concentration detector. Three designs of optically active element utilizing deformation of magnetic shape memory material in the external magnetic field were numerically simulated. Two designs (photonic crystal with cylindric holes in a hexagonal lattice and self-standing foil with cylindric holes in a square lattice) proved to be efficient and worth of further development.

Keywords: FDTD, Magneto-photonic crystal,Optical isolator, Concentration detector, magnetic shape memory alloy

Contents

Introduction

The magneto-optical effects play a crucial role in photonic technology, enabling light modulators, optical rotators, isolators, sensors, and numerous spectroscopic techniques. Lately, a significant effort was made to integrate optical isolators directly into Si technology, which would allow connecting the photonics and electronics. While the first attempt to integrate magneto-optical isolators to Si technology was performed based on ferrimagnetic garnets together with plasmonic technology [1], the industrially available technology is still missing. For the visible part of the spectrum, garnet technology is also used, but rather than using plasmonic nanostructures, photonic crystals are being employed to enhance the magneto-optical effect.

A photonic crystal is a periodic structure that exhibits similar properties for photons as an atomic crystal does for electrons. Its periodic structure is typically composed of various materials with different optical properties with high contrast in refractive index in various dimensions, as shown in figure 1.2. The periodicity in the refractive index behaves similarly as a periodic potential in atomic crystals.

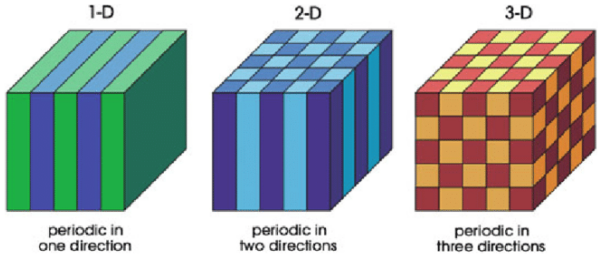

Figure 1: Example of photonic crystals with various dimensions of periodicity. Different colors represent different materials. The illustration is taken from [2]

.

Based on the wavelength of the incident light, the photon can or can not propagate through the photonic crystal, forming allowed and forbidden photonic bands. These bands are usually the result of destructive interference originating from the periodic nature of the refractive index variation. Light propagating in allowed photonic bands forms modes that can enhance a broad spectrum of physical phenomena due to their strong localization. Spectral regions corresponding to the forbidden bands exhibit a high valuse of reflectivity since the light can not propagate through the material. Several examples of this phenomena can include brag-mirrors, low-loss-waveguides, or various detectors. The periodicity of the photonic crystal should be in a scale comparable with half of the wavelength of the incident light to form these modes. For visible light it means lattice constant $a \in (190, 350)$ nm. These dimensions are relatively complicated to fabricate. But as long as the periodicity stays in scales comparable to the wavelength, these phenomena still occur to some degree.

When the photonic crystal is made from a magnetic material, its optical response can be modified by the presence of a magnetic field. Such crystal is called a magneto-photonic crystal.

Photonic crystals can be observed even in nature, as shown in figure 2.

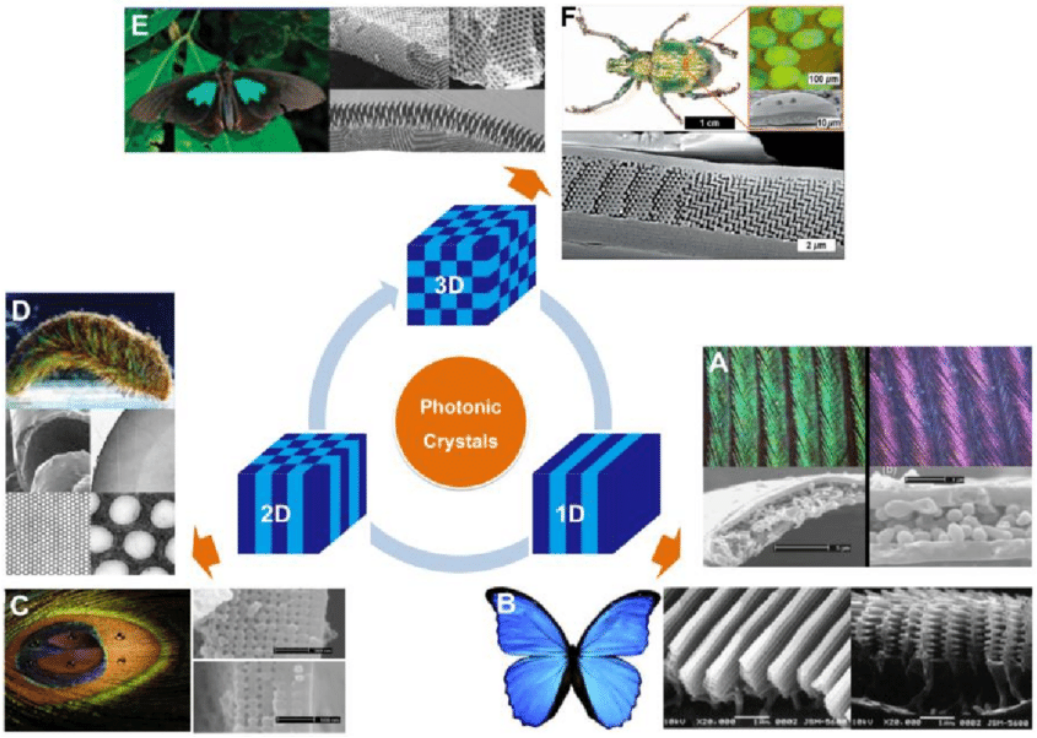

Figure 2: Examples of occurrence of photonic crystals in nature. 1-dimensional structures can be found at the green and purple neck feathers of domestic pigeons, another at Morpho butterflies. Colorful eyes on male peacock feathers are the product of two-dimensional photonic crystals. 3D inverse opal structures appearing in the green color of Parides sesostris, etc... The illustration is taken from [3].

Furthermore, ferromagnetic shape memory alloy (FSMA) [4] such as NiMnGa exhibits a significant deformation under the effect of the magnetic field. This deformation leads to the change of the geometry of the photonic crystal and thus affects its optical properties. Possible applications are magnetic field/deformation detectors, dynamic switches, optically active photonic elements, etc.

This thesis aims to (i) design and optimize the proper geometry of magneto-photonic crystal based on ferromagnetic garnet in order to resonantly enhance the magneto-optical response, (ii) to explore the possibility of using FSMA to build an optically active photonic element. For this purpose, advanced numerical modeling based on the Finite difference time domain (FDTD) method will be used. The FDTD calculations are carried out using LUMERICAL software, and further post-processing is done in PYTHON.

This thesis is divided into the following chapters.

Required magneto-optical variables are briefly summarized in the first chapter. The FDTD method for magnetooptics is briefly explained in the second chapter. Since magneto-optical effect requires off-diagonal elements in the tensor of permittivity and the FDTD method operates with constitutive relation in diagonal form, diagonalization and grid transformation are required. The third chapter is devoted to the design and optimization of a photonic rotator. The initial design

is based on garnet technology, and the numerical calculations are carried through the FDTD method. Within this chapter, a great enhancement of the Faraday rotation was found for a multi-layered photonic crystal. During an investigation of the origin of this enhancement, strongly localized modes were found, which led to an idea of a concentration detector, that is discussed, together with a proof of a concept, at the end of the chapter. In the last chapter, we demonstrate a magnetically controlled dynamic photonic crystal. Three different designs of a deformation detector based on the change in reflectivity are shown.

Part I

Theoretical background

1. Light polarisation and Magnetooptical variables

1.1 Polarisation ellipse

The light polarisation will be derived from Maxwell's equations:

$$\mathrm{rot}\,\boldsymbol{H} - \partial_t \boldsymbol{D} = \boldsymbol{j} \tag{1.1}$$

$$\mathrm{rot}\,\boldsymbol{E} + \partial_t \boldsymbol{B} = 0 \tag{1.2}$$

$$\mathrm{div}\,\boldsymbol{D} = \rho_e \tag{1.3}$$

$$\mathrm{div}\,\boldsymbol{B} = 0, \tag{1.4}$$

where $\boldsymbol{H}$ is the vector of magnetic field strength, $\boldsymbol{D}$ is the electric displacement vector, $\boldsymbol{j}$ is the electric current density vector, ρ_e is the electric charge density, $\boldsymbol{E}$ is the electric field strength vector, $\boldsymbol{B}$ is the magnetic flux density vector.

To describe the polarization of the light, it is better to simplify these equations by assuming a propagation in non-dispersive, non-conductive, homogenous, isotropic medium without charge density (ideal dielectric). In this medium:

$$\begin{aligned} \boldsymbol{j} &= 0 \\ \rho_e &= 0 \end{aligned} \tag{1.5}$$

$$\begin{aligned} \boldsymbol{D} &= \varepsilon \boldsymbol{E} \\ \boldsymbol{B} &= \mu \boldsymbol{H}, \end{aligned} \tag{1.6}$$

where ε is generally a permittivity tensor, and μ is generally a permeability tensor. In this case, however, with the assumptions we made, both tensors reduce to simple scalars. Equations 1.6 are called *electromagnetic Constitutive relations*.

Applying the rotation to the equation 1.2 and inserting it into equation 1.1, using the constitutive relation and using a vector identity:

$$\nabla \times \nabla \times \boldsymbol{A} = \nabla \cdot \nabla \boldsymbol{A} - \Delta \boldsymbol{A} \tag{1.7}$$

with the equation 1.3, we can derive wave equation:

$$\Delta \boldsymbol{E} - \varepsilon\mu \frac{\partial^2 \boldsymbol{E}}{\partial t^2} = 0. \tag{1.8}$$

Comparing this equation with the standard wave equation from mathematics, we can identify the term $\varepsilon\mu$ as $1/v^2$, where v is the wave's propagation speed in the medium.

We can define the coordinate system so that the z-direction is the direction of the propagation of the light. Thus $E_z = 0$ and we consider a solution for the remaining components in the form of plane wave:

$$\begin{aligned} E_x &= E_{x0}\cos\Big[\omega(t - \frac{z}{v}) + \delta_x\Big] \\ E_y &= E_{y0}\cos\Big[\omega(t - \frac{z}{v}) + \delta_y\Big] \end{aligned} \tag{1.9}$$

We proceed with substitution:

$$\tau = \omega(t - \frac{z}{v}). \tag{1.10}$$

Multipliing the first equation in 1.9 by $\sin\delta_y$ or $\cos\delta_y$ and the second by $\sin\delta_x$ or $\cos\delta_x$, substructing them and manipulating the terms, we obtain the following set of equations:

$$\begin{aligned} \frac{E_x}{E_{x0}}\sin\delta_y - \frac{E_y}{E_{y0}}\sin\delta_x &= \cos\tau(\cos\delta_x\sin\delta_y - \cos\delta_y\sin\delta_x) \\ \frac{E_x}{E_{x0}}\cos\delta_y - \frac{E_y}{E_{y0}}\cos\delta_x &= \sin\tau(\cos\delta_x\sin\delta_y - \cos\delta_y\sin\delta_x). \end{aligned} \tag{1.11}$$

The right hand side of these equations is equal to $\cos\tau\sin(\delta_y - \delta_x)$. The argument is a phase difference $\delta = \delta_y - \delta_x$. Summing the square of both equations in 1.11, we obtain:

$$\left(\frac{E_x}{E_{x0}}\right)^2 - 2\frac{E_x}{E_{x0}}\frac{E_y}{E_{y0}}\cos\delta + \left(\frac{E_y}{E_{y0}}\right)^2 = \sin^2\delta. \tag{1.12}$$

The equation 1.12 is an equation of ellipse oriented so that there is an angle ψ between the major axis of the ellipse and the x-axis. This angle fulfills the following relation:

$$\mathrm{tg}2\psi = \frac{2E_{x0}E_{y0}}{E_{x0}^2 - E_{y0}^2}\cos\delta \tag{1.13}$$

This means that the endpoint of the vector $\boldsymbol{E}$ describes the ellipse that lies in a plane perpendicular to the direction in which the light propagates. The ellipse is called the polarisation ellipse, and it can be characterized by four parameters. Three parameters can be used in case we are not interested in the initial phase. One of the possible combinations of these parameters is the set described in [5], which is visualized in figure 1.1. The polarisation vector will be defined as the direction of the electric field $\boldsymbol{E}$ because the electric field is the dominating field in the light-matter interaction. The rest of the field vectors $\boldsymbol{B}$, $\boldsymbol{D}$, and $\boldsymbol{H}$ can then be found using Maxwell's equations.

The polarisation ellipse is ilustrated of figure 1.1.

- $\psi \in [-\frac{\pi}{2}, \frac{\pi}{2})$ is the azimuthal angle oriented between the x-axis and the major axis of the ellipse.

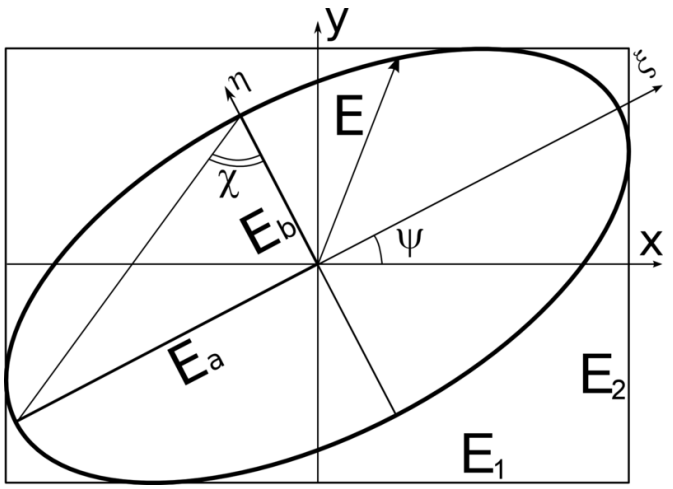

Figure 1.1: Polarization ellipse. The illustration is taken from [6]

.

- χ is a complementary ellipticity angle and is defined as $\frac{\pi}{2} - \varepsilon$, where $\varepsilon \in [-\frac{\pi}{4}, \frac{\pi}{4}]$ is an ellipticity angle. From these angles, the elipticity $e \in [-1, 1]$ can be calculated as $e = \pm\frac{E_b}{E_a} = tg\varepsilon$. E_a and E_b is the lenght of the semi-major and semi-minor axis respectively.
- The third parameter is the amplitude $A_{00} = \sqrt{E_a^2 + E_b^2}$ of the field, which measures the strength of the eliptical vibration.
- The last parameter required to describe the polarized state is the absolute phase $\delta_0 \in [-\pi, \pi)$, that measures the angle between the initial position of the electric field, meaning $\boldsymbol{E} = \boldsymbol{E}_{(t=0)}$, and the major axis of the ellipse.

The focus of this thesis will revolve around the calculation of the azimuthal angle ψ.

1.2 Magneto-Optical Effects

A magneto-optical effect is a phenomenon of the electromagnetic wave that propagates through a medium exposed to a magnetic field. Such exposure induces an optical anisotropy in the material, which can be described by off-diagonal elements in the permittivity tensor. Such medium is called *gyrotropic / gyromagnetic* [7]. An electromagnetic wave that can be decomposed into left- and right elliptically polarized waves experiences a different refractive index for both polarisations, and thus each polarisation propagates with a different velocity. This difference in the propagation speed causes one polarisation to "lack behind" and thus gain a phase difference compared to the other polarisation. This produces a polarisation rotation by propagation through magnetized material. The magnetic field can be external or internal (ferromagnetic).

The relation between the displacement vector and the electric field can be written as:

$$\begin{aligned} \mathbf{D} &= \varepsilon\mathbf{E} = \varepsilon'\mathbf{E} + i\mathbf{E} \times \mathbf{g} \\ \mathbf{g} &= \varepsilon_0\chi^m\mathbf{H} \end{aligned} \tag{1.14}$$

The ε' is a real symmetric tensor. Pseudovector $\mathbf{g}$ is called *gyration vector*. Its magnitude is generally significantly smaller than the eigenvalues of ε' [7]. χ^m is a magneto-optical susceptibility, which is a tensor for anisotropic media.

In this thesis, we will use the simplest case, when the g lies in the direction of the principal axis of the ε'. We are working with materials that are isotropic without the presence of the magnetic field. This means that they can be represented by a scalar permittivity. While under exposure to the magnetic field, the dielectric tensor takes the form of:

$$\varepsilon = \begin{pmatrix} \varepsilon_1 & +ig_z & 0 \\ -ig_z & \varepsilon_1 & 0 \\ 0 & 0 & \varepsilon_1 \end{pmatrix} \tag{1.15}$$

For a lossy medium, both diagonal and off-diagonal components have to be complex.

1.2.1 Faraday Rotation

Faraday rotation ψ is an angle produced by the magneto-optical Kerr effect. The angle is defined as a difference between the polarisation angle of the incoming wave and a wave that propagate through the material:

$$\psi_f = \psi_{out} - \psi_{in}, \tag{1.16}$$

where ψ_{in} is the azimuthal angle of the input wave, ψ_{ou} is the azimuthal angle of the output wave, and ψ_f is the rotation angle.

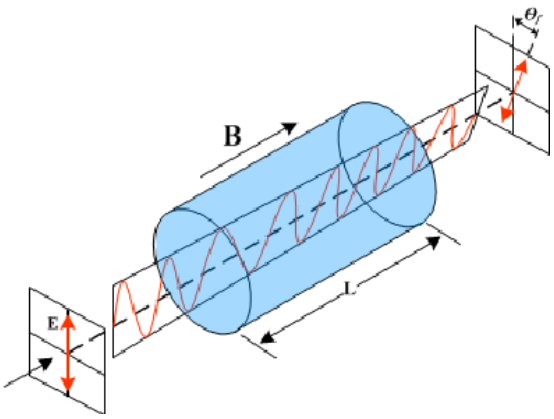

Figure 1.2: Schematic description of Faraday rotation of linearly polarized light. The illustration is taken from [8]

.

Because the phase difference between left and right circular polarisation, gained during the propagation, is proportional to the off-diagonal elements of the permittivity tensor, which are in the first order proportional to the magnetic field applied, the Faraday rotation can be simply characterized as:

$$\psi_f = VB_z d, \tag{1.17}$$

where B is the magnetic flux density, d is the thickness of the material, and V is a *Verdent constant* of the material [9]. By this definition, the rotation could exceed

$\psi_f = 180°$, which makes sense for homogenous materials, because reducing the thickness of the material leads to a proportional reduction in Faraday rotation to values under $\psi_f = 180°$. In our case, however, the rotating structure is a 2-D photonic crystal where reducing the thickness makes no sense, and thus we will work only with rotations lower than 180°.

1.2.2 Magneto-optical Kerr Effect

Another type of rotation of the polarisation is a Magneto-optical Kerr Effect (MOKE), which is similar to the Faraday effect because it also originates from off-diagonal elements of the permittivity tensor. MOKE, however, produces a change in polarisation angle during a reflection from the magnetized surface. Offdiagonal elements of the permittivity tensor produce anisotropy in permittivity, which results in anisotropy in reflection coefficient and speed of light for various directions:

$$c = \frac{1}{\sqrt{\varepsilon\mu}} \tag{1.18}$$

If the light in different directions can propagate with different speeds and feels different reflection coefficients, it gains a different phase shift, which results in a change of the polarisation angle.

2. Magnetooptical FDTD simulation

FDTD stands for the *Finite difference time domain* which is an approach to solve Maxwell's equations in a confined space.

2.1 Brief introduction into FDTD method

The whole FDTD algorithm is reasonably complex. This section aims not to describe the entire method but rather provide a general understanding and insight into the problem. To write the FDTD code, the previous author's thesis offers a guide on writing the algorithm to run on a graphic card with CUDA architecture using Python ([10]).

Another recommendation would be [11], where the author provides a descriptive derivation of the FDTD method in 1D, 2D, and 3D in programming language C together with some useful examples and offers an extension of this method to other branches of physics such as quantum mechanics.

Lastly, for an in-depth understanding of this method, we recommend a book [12], which focuses on an in-depth explanation of each component of the simulation and also provides examples in Matlab.

But do not be mistaken. Although previous authors used MATLAB or C to write the FDTD code, it is only a sub-optimal solution. With the rise of tools such as *PyTorch* or *Tensor Flow*, it is more efficient to use these tools instead because the evolution equation can be translated into convolutional form which is a natural for graphic cards.

2.1.1 Analytical evolution equations

Once again, we will start with the Maxwell's equations:

$$\begin{aligned} \operatorname{rot} \boldsymbol{H} - \partial_t \boldsymbol{D} &= \boldsymbol{j} \\ \operatorname{div} \boldsymbol{D} &= \rho_e \\ \operatorname{rot} \boldsymbol{E} + \partial_t \boldsymbol{B} &= -\boldsymbol{M} \\ \operatorname{div} \boldsymbol{B} &= \rho_m \end{aligned} \tag{2.1}$$

Here $\boldsymbol{H}$ stands for the magnetic field strength vector, $\boldsymbol{D}$ is the electric displacement vector, $\boldsymbol{j}$ is the electric current density vector, ρ_e is the electric charge density, $\boldsymbol{E}$ is the electric field strength vector, $\boldsymbol{B}$ is the magnetic flux density vector, $\boldsymbol{M}$ is the magnetic current density vector, and finally ρ_m is the magnetic charge density. Terms $\boldsymbol{M}$ and ρ_m are not physical entities. Their presence in the equations only helps to solve some problems more elegantly. We can simply ignore them by setting their value to 0.

To describe how do these fields interact with the material, we introduce constitutive relations:

$$\boldsymbol{D}(t) = \varepsilon(t) * \boldsymbol{E}(t), \tag{2.2}$$
$$\boldsymbol{B}(t) = \mu(t) * \boldsymbol{H}(t). \tag{2.3}$$

Next, we expand curl equations in 2.1 and introduce the dimension reduction. By that, we mean that there will be no changes in material nor fields in $\boldsymbol{z}$ direction and thus $\frac{\partial}{\partial z} = 0$:

$$\begin{aligned} \frac{\partial H_z}{\partial y} - \frac{\partial D_x}{\partial t} &= j_x \\ -\frac{\partial H_z}{\partial x} - \frac{\partial D_y}{\partial t} &= j_y \\ \frac{\partial H_y}{\partial x} - \frac{\partial H_x}{\partial y} - \frac{\partial D_z}{\partial t} &= j_z \end{aligned} \tag{2.4}$$

$$\begin{aligned} \frac{\partial E_z}{\partial y} + \frac{\partial B_x}{\partial t} &= -M_x \\ -\frac{\partial E_z}{\partial x} + \frac{\partial B_y}{\partial t} &= -M_y \\ \frac{\partial E_y}{\partial x} - \frac{\partial E_x}{\partial y} + \frac{\partial B_z}{\partial t} &= -M_z \end{aligned} \tag{2.5}$$

Now, we can split these sets of equations into two independent sets of equations called transversal magnetic (TM) and transversal electric (TE) modes respectively:

$$\begin{aligned} \frac{\partial D_z}{\partial t} &= \frac{\partial H_y}{\partial x} - \frac{\partial H_x}{\partial y} - j_z \\ \frac{\partial B_x}{\partial t} &= -\frac{\partial E_z}{\partial y} - M_x \\ \frac{\partial B_y}{\partial t} &= \frac{\partial E_z}{\partial x} - M_y \end{aligned} \tag{2.6}$$

$$\begin{aligned} \frac{\partial B_z}{\partial t} &= \frac{\partial E_x}{\partial y} - \frac{\partial E_y}{\partial x} - M_z \\ \frac{\partial D_x}{\partial t} &= \frac{\partial H_z}{\partial y} - j_x \\ \frac{\partial D_y}{\partial t} &= -\frac{\partial H_z}{\partial x} - j_y \end{aligned} \tag{2.7}$$

We will focus on deriving the evolution equations for TM mode only. The procedure for TE mode is the same. The next step is to add the constitutive relations. We will consider the simplified case of using diagonal permittivity and permeability.

$$\varepsilon = \begin{bmatrix} \varepsilon_x & 0 & 0 \\ 0 & \varepsilon_y & 0 \\ 0 & 0 & \varepsilon_z \end{bmatrix} \tag{2.8}$$

$$\mu = \begin{bmatrix} \mu_x & 0 & 0 \\ 0 & \mu_y & 0 \\ 0 & 0 & \mu_z \end{bmatrix} \tag{2.9}$$

Note that these tensors can still be time dependent. Even though the diagonal tensor forms seem like a strict limitation, and for magnetooptics, we actually need off-diagonal terms. There is a way around this which is described later in this thesis.

Now we use these constitutive relations to replace $\boldsymbol{B}$ with $\boldsymbol{H}$ and $\boldsymbol{D}$ with $\boldsymbol{E}$. Then we introduce a form of *Ohm's law*:

$$\begin{aligned} \boldsymbol{j} &= \boldsymbol{j}_c + \boldsymbol{j}_i = \sigma^e \boldsymbol{E} + \boldsymbol{j}_i \\ \boldsymbol{M} &= \boldsymbol{M}_c + \boldsymbol{M}_i = \sigma^m \boldsymbol{H} + \boldsymbol{M}_i \end{aligned} \tag{2.10}$$

Where σ^e (σ^m) is electric (magnetic) conductivity in a diagonal form:

$$\sigma^e = \begin{bmatrix} \sigma_x^e & 0 & 0 \\ 0 & \sigma_y^e & 0 \\ 0 & 0 & \sigma_z^e \end{bmatrix} \tag{2.11}$$

$$\sigma^m = \begin{bmatrix} \sigma_x^m & 0 & 0 \\ 0 & \sigma_y^m & 0 \\ 0 & 0 & \sigma_z^m \end{bmatrix} \tag{2.12}$$

Finally, we obtain:

$$\begin{aligned} \frac{\partial E_z}{\partial t} &= \frac{1}{\varepsilon_z}\Big(\frac{\partial H_y}{\partial x} - \frac{\partial H_x}{\partial y} - \sigma_z^e E_z - j_{iz}\Big) \\ \frac{\partial H_x}{\partial t} &= \frac{1}{\mu_x}\Big(-\frac{\partial E_z}{\partial y} - \sigma_x^m H_x - M_{ix}\Big) \\ \frac{\partial H_y}{\partial t} &= \frac{1}{\mu_y}\Big(\frac{\partial E_z}{\partial x} - \sigma_y^m H_y - M_{iy}\Big), \end{aligned} \tag{2.13}$$

which is the correct form of the analytical evolution equations to proceed into the next step.

2.1.2 Finite step approximation

This is the crucial step that stands behind the whole method. Now we replace derivatives with differences. A derivative is defined as:

$$f'(x) = \lim_{\Delta x \to 0} \frac{f(x + \Delta x) - f(x)}{\Delta x}. \tag{2.14}$$

However, we can not make the Δx infinitely small, the step has to be finite, and so we can only approximate this formula. The most common way to do it is this:

$$f'(x) \approx \frac{f(x + \Delta x) - f(x - \Delta x)}{2\Delta x}. \tag{2.15}$$

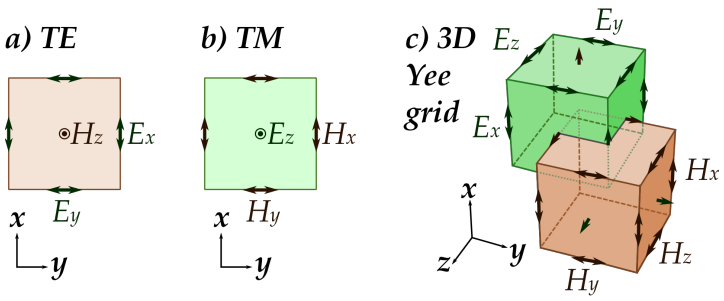

Figure 2.1: YEE grid shift

Now, Δx is fixed and represents an elementary cell size in an orthogonal grid. Note that we are evaluating a function at x based on other function at $x + \Delta x$ and $x - \Delta x$, but not at x itself.

To justify this approximation, we need to choose the Δx (and Δt) correctly:

$$\Delta x = 2\, c_0 \Delta t, \tag{2.16}$$

where c_0 is the speed of light in a vacuum.

This did not help much because we still need to set a Δt so that the simulation would have a good convergency. A way to do that is to choose Δt so that it takes the wave 10 - 20 time steps to propagate through a single cell in the simulation. Note that the propagation time varies in different media, so this has to be chosen based on the material with the highest speed of propagation.

The next step is to apply this approximation to equations 2.13. Since the derivative uses only every other cell to evaluate a cell in the new time step and there is a two-cell step in the fraction's denominator (equation 2.15), we can make the grid twice as delicate while keeping the same amount of field cells. This results in a spatial shift of the magnetic field grid to the electric field grid:

$$\begin{aligned} E_z(i,\, j) &\Rightarrow \Big[i\Delta x,\, j\Delta y\Big] \\ H_x(i,\, j) &\Rightarrow \Big[i\Delta x,\, (j+0.5)\Delta y\Big] \\ H_y(i,\, j) &\Rightarrow \Big[(i+0.5)\Delta x,\, j\Delta y\Big], \end{aligned} \tag{2.17}$$

or more illustratively shown in2.1. This shifted grid is called *YEE grid* [12].

Now we can transform the 2.13 into a difference equation on the YEE grid:

$$\begin{aligned} \frac{E_z^{n+1}(i,\, j) - E_z^{n}(i,\, j)}{\Delta t} = &\frac{1}{\varepsilon_z(i,\, j)} \frac{H_y^{n+\frac{1}{2}}(i,\, j) - H_y^{n+\frac{1}{2}}(i-1,\, j)}{\Delta x} \\ &- \frac{1}{\varepsilon_z(i,\, j)} \frac{H_x^{n+\frac{1}{2}}(i,\, j) - H_x^{n+\frac{1}{2}}(i,\, j-1)}{\Delta y} \\ &- \frac{\sigma_z^e(i,\, j)}{\varepsilon_z(i,\, j)} E_z^{n+\frac{1}{2}}(i,\, j) - \frac{j_{iz}^{n+\frac{1}{2}}(i,\, j)}{\varepsilon_z(i,\, j)} \end{aligned} \tag{2.18}$$

$$\begin{aligned}\frac{H_x^{n+\frac{1}{2}}(i,\,j)-H_x^{n-\frac{1}{2}}(i,\,j)}{\Delta t} &= -\frac{1}{\mu_x(i,\,j)}\frac{E_z^n(i,\,j+1)-E_z^n(i,\,j)}{\Delta y}\\ &\quad -\frac{\sigma_x^m(i,\,j)}{\mu_x(i,\,j)}H_x^n(i,\,j)-\frac{M_{ix}^n(i,\,j)}{\mu_x(i,\,j)}\end{aligned} \tag{2.19}$$

$$\begin{aligned}\frac{H_y^{n+\frac{1}{2}}(i,\,j)-H_y^{n-\frac{1}{2}}(i,\,j)}{\Delta t} &= \frac{1}{\mu_y(i,\,j)}\frac{E_z^n(i+1,\,j)-E_z^n(i,\,j)}{\Delta x}\\ &\quad -\frac{\sigma_y^m(i,\,j)}{\mu_y(i,\,j)}H_y^n(i,\,j)-\frac{M_{iy}^n(i,\,j)}{\mu_y(i,\,j)}\end{aligned} \tag{2.20}$$

The upper index at field variables stands for the time step. We want to use integers for indexing time steps for electric field and integers$+\frac{1}{2}$ for indexing magnetic field. The first term on the third line in 2.18 for the electric field, however, does not have an integer value, and the same problem stands for several variables of the magnetic field. Thus, we approximate the value by:

$$\begin{aligned}E_z^{n+\frac{1}{2}} &\approx \frac{E_z^n+E_z^{n+1}}{2}\\ H_x^n &\approx \frac{H_x^{n+\frac{1}{2}}+H_x^{n-\frac{1}{2}}}{2}\\ H_y^n &\approx \frac{H_y^{n+\frac{1}{2}}+H_y^{n-\frac{1}{2}}}{2}\end{aligned} \tag{2.21}$$

Using these substitutions, we can express the field variable in a new step from variables of the previous time steps:

$$\begin{aligned}E_z^{n+1}(i,\,j) &= \frac{4\varepsilon_0\varepsilon_{rz}(i,\,j)c_0-\sigma_z^e(i,\,j)\Delta x}{4\varepsilon_0\varepsilon_{rz}(i,\,j)c_0+\sigma_z^e(i,\,j)\Delta x}E_z^n(i,\,j)\\ &\quad +\frac{2}{4\varepsilon_0\varepsilon_{rz}(i,\,j)c_0+\sigma_z^e(i,\,j)\Delta x}\left[H_y^{n+\frac{1}{2}}(i,\,j)-H_y^{n+\frac{1}{2}}(i-1,\,j)\right]\\ &\quad -\frac{2k}{4\varepsilon_0\varepsilon_{rz}(i,\,j)c_0+\sigma_z^e(i,\,j)\Delta x}\left[H_x^{n+\frac{1}{2}}(i,\,j)-H_x^{n+\frac{1}{2}}(i,\,j-1)\right]\\ &\quad -\frac{2\Delta x}{4\varepsilon_0\varepsilon_{rz}(i,\,j)c_0+\sigma_z^e(i,\,j)\Delta x}j_{iz}^{n+\frac{1}{2}}(i,\,j)\end{aligned} \tag{2.22}$$

$$\begin{aligned}H_x^{n+\frac{1}{2}}(i,\,j) &= \frac{4c_0\mu_0\mu_{rx}(i,\,j)-\Delta x\sigma_x^m(i,\,j)}{4c_0\mu_0\mu_{rx}(i,\,j)+\Delta x\sigma_x^m(i,\,j)}H_x^{n-\frac{1}{2}}(i,\,j)\\ &\quad -\frac{2k}{4c_0\mu_0\mu_{rx}(i,\,j)+\Delta x\sigma_x^m(i,\,j)}\left[\tilde{E}_z^n(i,\,j+1)-\tilde{E}_z^n(i,\,j)\right]\\ &\quad -\frac{2\Delta x}{4c_0\mu_0\mu_{rx}(i,\,j)+\Delta x\sigma_x^m(i,\,j)}M_{ix}^n(i,\,j)\end{aligned} \tag{2.23}$$

$$
\begin{aligned}
H_y^{n+\frac{1}{2}}(i,\,j) = &\frac{4c_0\mu_0\mu_{ry}(i,\,j) - \Delta x\sigma_y^m(i,\,j)}{4c_0\mu_0\mu_r(i,\,j) + \Delta x\sigma_y^m(i,\,j)} H_y^{n-\frac{1}{2}}(i,\,j) \\
&+ \frac{2}{4c_0\mu_0\mu_{ry}(i,\,j) + \Delta x\sigma_y^m(i,\,j)}\Big[\tilde{E}_z^n(i+1,\,j) - \tilde{E}_z^n(i,\,j)\Big] \\
&- \frac{2\Delta x}{4c_0\mu_0\mu_{ry}(,\,j) + \Delta x\sigma_y^m(i,\,j)} M_{iy}^n(i,\,j).
\end{aligned}
\tag{2.24}
$$

This might look a little intimidating, but these equations are rather simple from the programming point of view. Fractions in front of the field differences can be substituted by values that can be precomputed before the main part of the algorithm.

$$
\begin{aligned}
\tilde{E}_z^{n+1}(i,\,j) = &\, C_{ezez}(i,\,j)\tilde{E}_z^n(i,\,j) \\
&+ C_{ezhy}(i,\,j)\Big[H_y^{n+\frac{1}{2}}(i,\,j) - H_y^{n+\frac{1}{2}}(i-1,\,j)\Big] \\
&- C_{ezhx}(i,\,j)\Big[H_x^{n+\frac{1}{2}}(i,\,j) - H_x^{n+\frac{1}{2}}(i,\,j-1)\Big] \\
&- C_{ezjiz}(i,\,j)j_{iz}^{n+\frac{1}{2}}(i,\,j) \\
H_x^{n+\frac{1}{2}}(i,\,j) = &\, C_{hxhx}(i,\,j)H_x^{n-\frac{1}{2}}(i,\,j) \\
&- C_{hxez}(i,\,j)\Big[\tilde{E}_z^n(i,\,j+1) - \tilde{E}_z^n(i,\,j)\Big] \\
&- C_{hxmix}(i,\,j)M_{ix}^n(i,\,j) \\
H_y^{n+\frac{1}{2}}(i,\,j) = &\, C_{hyhy}(i,\,j)H_y^{n-\frac{1}{2}}(i,\,j) \\
&+ C_{hyez}(i,\,j)\Big[\tilde{E}_z^n(i+1,\,j) - \tilde{E}_z^n(i,\,j)\Big] \\
&- C_{hymiy}(i,\,j)M_{iy}^n(i,\,j)
\end{aligned}
\tag{2.25}
$$

Equations 2.25 are the final form of the evolution equations. The field variable in the new time step is calculated based on field variables at previous time steps. We could modify these equations further into convolution form, but that would only complicate its form, and the illustrative purpose would be lost.

2.1.3 Boundary conditions

Although this algorithm is fairly robust, there is still a problem at the edge of the grid. Cells at the edge of the grid miss one or more neighboring cells to compute the field's value in the following time step. If left unchecked, this would produce unwanted reflection, which would travel back into the simulation space, causing unwanted signal in the simulation.

Several approaches try to eliminate these reflections. One of them is a *Perfectly matched layer* (PML) which adds an additional layer around the YEE grid, which is made of an artificial material that matches perfectly in impedance with the inside grid but is lossy. So the wave decays as it travels within the layer. It reflects at the new outer boundary and travels back through the lossy medium

again, resulting in a reduction in the reflection in several orders of magnitude. The matching condition is set so that:

$$\Gamma = \frac{\eta_A - \eta_B}{\eta_A + \eta_B}, \tag{2.26}$$

where η is the impedance of respective medium:

$$\eta = \sqrt{\frac{\mu}{\varepsilon}}. \tag{2.27}$$

From a practical point of view, this means that there has to be an additional variable in the whole simulation representing this artificial loss. This variable has to be zero inside the simulation space and gradually increase in the PML layers, satisfying the impedance matching condition. This topic is discussed in greater detail in [11] or [12].

There are many different types of boundary conditions. Missing cells can be replaced by values on the opposite side of the grid, resulting in periodic boundary conditions, which could be symmetric or antisymmetric. These boundary conditions can be combined so that each side of the simulations uses different conditions, allowing us to exploit the problem's symmetry and reduce the simulation area, which results in higher computational power.

2.1.4 Object representation

Building an object on the Yee-grid presents a new challenge. The grid is finite and orthogonal, while the object can be oblique with dimensions that do not match cell-size multiplicity.

Another problem is that electric and magnetic field variables are shifted in space by half of the cell size, so approximating the object has to be done for each field separately.

Furthermore, the method works in the time domain, which means that it produces a whole spectrum at once. In the derivation of evolution equations, we assumed non-dispersive material, but that is a strict restriction. In reality, we need to specify $\varepsilon_{(\omega)}$ and $\mu_{(\omega)}$ and somehow incorporate that into the simulation.

The first start of this problem can be simply solved by a filling factor representing how much volume each material occupies in a cell and then use a weighted average for the calculation of the material data in that cell. This is not an ideal solution. However, there are other approaches with faster convergency (in terms of grid delicacy)

A more sophisticated approach would be to build the object on a more detailed grid (10 times or more), then blur the image by convolving it by a pixel of the final grid's size with normalized value. Project this blurred data into the final grid and in each cell, take the value in the middle. (Figure 2.2)

The thing that has to be kept in mind is that electric and magnetic fields are represented by separate grids that are shifted in space, and so the process described above has to be done for each grid separately. (See picture 2.3)

Simulating the frequency dependent optical response of a material requires parametrization the material data by some analytical function. The function itself modifies the evolution equation, and so in commercial software, such as

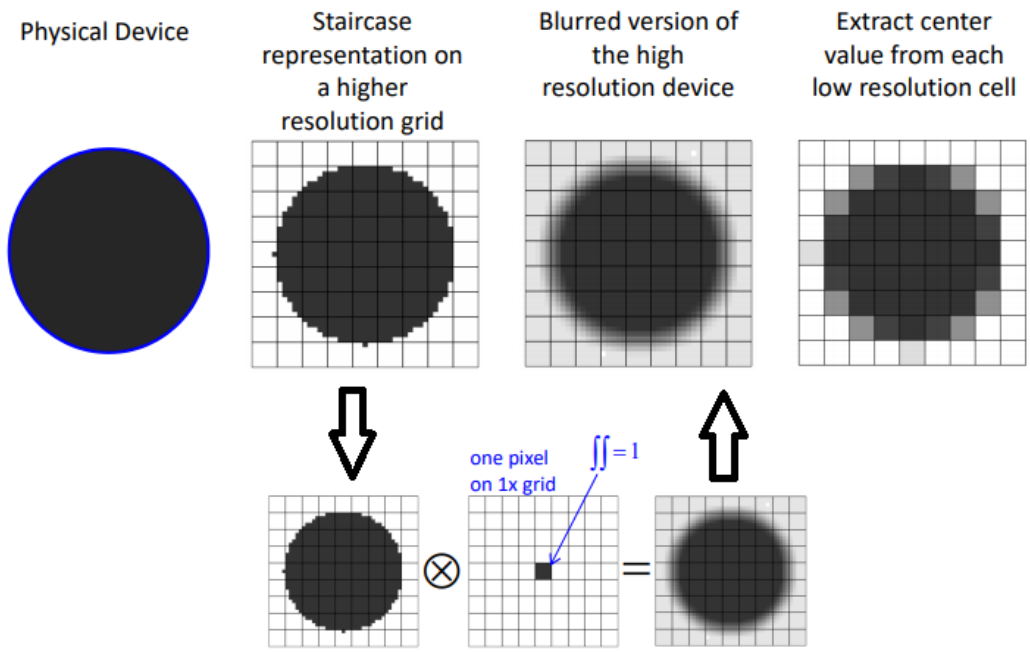

Figure 2.2: Smoothing procedure, using the detailed grid technique and convolution. This picture is taken from [13].

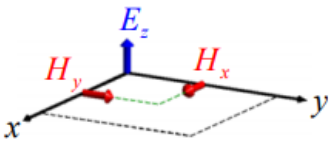

Figure 2.3: Electric and magnetic field vector components spatial position in TM mode. This picture is taken from [13].

Lumerical, the type of the parametrization function can not be changed. Lumerical uses polynomial fit, but for our demonstrative purposes, we will use a *Debye formulation*:

$$\varepsilon_r^* = \varepsilon_r + \frac{\sigma}{i\omega\varepsilon_0} + \frac{\chi_1}{1 + i\omega t_0}, \tag{2.28}$$

where ε_r^* is the frequency-dependent relative dielectric constant, ε_r (sometimes noted as $\varepsilon_r(\infty)$ is a constant high-frequency contribution to the dielectric function, σ is a conductivity and χ_1 is a Debye fit parameter.

$$D(\omega) = \varepsilon_r \cdot E(\omega) + \frac{\sigma}{i\omega\varepsilon_0} \cdot E(\omega) + \frac{\chi_1}{1 + i\omega t_0} \cdot E(\omega) \tag{2.29}$$

The method operates in the time domain, so we have to map the frequency dependent terms to the time domain using a *Fourier tranform*:

$$D(t) = \varepsilon_r \cdot E(t) + \frac{\sigma}{\varepsilon_0} \int_0^t E(t') \cdot dt' + \frac{\chi_1}{t_0} \int_0^t e^{-(t'-t)/t_0} E(t') \cdot dt' \tag{2.30}$$

The integration starts at $t' = 0$ because we assume that the simulation starts at $t = 0$ and source fields are zero initially; thus, there can be no influence from times $t' < 0$.

In discrete domain, we obtain:

$$D^n = \varepsilon_r \cdot E^n + \frac{\sigma \cdot \Delta t}{\varepsilon_0} \sum_{i=0}^{n} E^i + \frac{\chi_1 \cdot \Delta t}{t_0} \sum_{i=0}^{n} e^{-\Delta t(n-i)/t_0} E^i \tag{2.31}$$

Calculating the whole sums in every time step would be numerically demanding. We can introduce additional variables that will hold the value of the sum and update it every step:

$$\begin{aligned} D^n &= \varepsilon_r \cdot E^n + \frac{\sigma \cdot \Delta t}{\varepsilon_0} E^n + I^{n-1} + \frac{\chi_1 \cdot \Delta t}{t_0} E^i + S^{n-1} \\ I^n &= \frac{\sigma \cdot \Delta t}{\varepsilon_0} \sum_{i=0}^{n} E^i = I^{n-1} + \frac{\sigma \cdot \Delta t}{\varepsilon_0} E^n \\ S^n &= \frac{\chi_1 \cdot \Delta t}{t_0} \sum_{i=0}^{n} e^{-\Delta t(n-i)/t_0} E^i = e^{-\Delta t/t_0} S^{n-1} + \frac{\chi_1 \cdot \Delta t}{t_0} E^i \end{aligned} \tag{2.32}$$

With these equations, we can now write a $E^n = f(D^n, I^{n-1}, S^{n-1})$ with their updating equations:

$$\begin{aligned} E^n &= \frac{D^n - I^{n-1} - e^{-\Delta t/t_0} S^{n-1}}{\varepsilon_r + \frac{\sigma \cdot \Delta t}{\varepsilon_0} + \frac{\chi_1 \cdot \Delta t}{t_0}} \\ I^n &= I^{n-1} + \frac{\sigma \cdot \Delta t}{\varepsilon_0} E^n \\ S^n &= e^{-\Delta t/t_0} S^{n-1} + \frac{\chi_1 \cdot \Delta t}{t_0} E^i \end{aligned} \tag{2.33}$$

Originaly, the core of the algorithm worked like this:

- Update $E^n(E^{n-1}, H^n)$
- Update $H^n(E^n, H^{n-1})$

For dispersive medium, we can not insert the constitutive relations into the evolution equations, and thus, the core of the algorithm looks as follows:

- Update $D^n(D^{n-1}, H^n)$ Updating equation for electric field
- Update $E^n(D^n, I^n)$ Constitutive relation for electric field
- Update $I^n(I^{n-1}, E^n)$ Supportive equation for the first term of the material fit
- Update $S^n(S^{n-1}, E^n)$ Supportive equation for the second term of the material fit
- Update $H^n(H^{n-1}, E^n)$ Updating equation for the magnetic field

2.1.5 Field input and output

The last thing we need to mention in this brief overview of the FDTD method is how the wave source is implemented and how the data are collected.

The method operates in the time domain and thus offers us to calculate a continuous part of the spectrum at once. To do so, we have to illuminate the simulation area with a pulse that contains all the wavelengths we are interested in.

A suitable profile of the source pulse can have a gaussian shape in the time domain. If we apply a Fourier transform to such pulse, we end up with a rescaled gaussian shape, but in the frequency domain. (See equation 2.35)

In this thesis, we define the Fourier transform ($\mathcal{F}.\mathcal{T}.$) as:

$$\begin{aligned} F(\omega) &= \frac{1}{\sqrt{2\pi}} \int_{-\infty}^{\infty} f(t) \cdot e^{i\omega t} dt \\ f(t) &= \frac{1}{\sqrt{2\pi}} \int_{-\infty}^{\infty} F(\omega) \cdot e^{-i\omega t} dt \end{aligned} \tag{2.34}$$

which results in:

$$\mathcal{F}.\mathcal{T}.\ ae^{\frac{t^2}{b}} = \frac{a}{\sqrt{2\pi}} \int_{-\infty}^{\infty} e^{\frac{t^2}{b}} \cdot e^{i\omega t} dt = \frac{ae^{-\frac{1}{4}\left(b\omega^2\right)}}{\sqrt{2}\sqrt{\frac{1}{b}}} \tag{2.35}$$

If we want, for example, to calculate a transmission of a simulated device, we can record the data of a field at some point, line, or plane, calculate the Fourier transform of the output, and then divide it by the Fourier transform of the input.

Since the FDTD provides the entire set electromagnetic field vectors value during the whole simulation, coupling the simulation with the right kind of post-processing makes the FDTD one of the most versatile numerical methods.

2.2 Grid attribute

The implementation of magneto-optical effects into FDTD simulations brings in some difficulties. Material tensors in constitutive relations now have some off-diagonal elements, but the commercial algorithm only works with diagonal tensors. Introducing off-diagonal elements into evolution equations would lead to a drastic increase in their complexity, and thus, the computer memory and computational time requirement would also increase. Luckily, this can be avoided by using diagonalization of the constitutive tensors utilizing a unitary transformation:

$$\boldsymbol{\varepsilon}_D = \boldsymbol{U}\boldsymbol{\varepsilon}\boldsymbol{U}^{\dagger}, \tag{2.36}$$

where

$$\boldsymbol{U} = \boldsymbol{V}^{\dagger}, \tag{2.37}$$

while $\mathbf{V}$ is the eigenvector matrix of ε. We can then introduce a grid attribute that locally rotates the grid, using the $\mathbf{V}$ tensor, which effectively reintroduces

the off-diagonal terms into the simulation, and so using these two transformations together, we get a simulation that behaves as if we would work with off-diagonal constitutive tensor while having to work only with a diagonal version.

2.2.1 Grid attribute for MOKE

Having the matrial data $\varepsilon_{(\omega)}$ in a form of:

$$\boldsymbol{\varepsilon}_{(\omega)} = \begin{bmatrix} a+ib & c+id & 0 \\ -c-id & a+ib & 0 \\ 0 & 0 & a+ib \end{bmatrix}, \tag{2.38}$$

Where a, b, c, d are the functions of ω, we obtain the unitary matrix $\boldsymbol{U}$ in the following form:

$$\boldsymbol{U} = \frac{1}{\sqrt{2}} \begin{bmatrix} 0 & 0 & \sqrt{2} \\ i & 1 & 0 \\ -i & 1 & 0 \end{bmatrix}. \tag{2.39}$$

This yields

$$\boldsymbol{\varepsilon}_D = \begin{bmatrix} a+ib & 0 & 0 \\ 0 & a+ib-i(c+id) & 0 \\ 0 & 0 & a+ib+i(c+id) \end{bmatrix}, \tag{2.40}$$

which is a diagonal form of a constitutive relation, suitable for efficient FDTD simulation.

2.2.2 Grid attribute for Faraday

To simulate the Faraday effect, one option is to take a anisotropic material with diagonal tensor and introduce a new grid attribute, that locally rotates the reference frame such that it converts the field components from Cartesian coordinates into coordinates that represent circular polarisation. This can be done by introducing additional unitary transformation, represented by the following matrix $\boldsymbol{W}$ [14]:

$$\boldsymbol{W} = \frac{1}{\sqrt{2}} \begin{bmatrix} 1 & 0 & i \\ 0 & \sqrt{2} & 0 \\ 1 & 0 & -i \end{bmatrix}, \tag{2.41}$$

In our case, however, we have a diagonally isotropic material with off-diagonal components already introduced, and so we can use the same grid attribute as in MOKE simulation $\boldsymbol{U}$.

2.3 The Faraday rotation calculation

Instead of calculating the Faraday rotation directly, the polarisation ellipse has to be calculated first. This is because the off-diagonal permittivity terms results in generally elliptically polarized light. The azimuthal angle ψ is then used as the Faraday rotation angle.

Calculating the polarisation ellipse from FDTD simulation requires a calculation of far-field components (a field outside of the simulation region, which is so far that evanescent waves does not contribute) within the post-processing. In the Lumerical, there is already a function for this, but for our purposes, the script had to be modified so that the polarisation ellipse is calculated only from the first grating order. Another required modification was the form of the output which originally calculated the polarisation ellipse just for a single wavelength, but in this thesis, we are interested in the whole spectrum.

The monitor (strip of the grid cells that records data) for the far-field calculation is located 3 μm below the simulation interest point. The median period of photonic crystals investigated in this thesis is around 1000 nm, and the spectral region in interest is around 460 nm. This is a zone where evanescent waves are sufficiently small, and the simulation area is not yet stretched into sizes that are hard to work with. For some simulations in higher resolution, the monitor is placed only 1 μm under the point of interest to reduce the overall simulation area and thus to reduce the simulation's hardware requirements. A convergence test was made to justify the placement of the monitor.

In other cases, the Faraday rotation could also be calculated directly from the near field monitors, using the integration of corresponding field components over the surface. However, in this case, no matter how far the monitor is placed, there will always be all the grating order components of the field. This is because we are using periodic boundary conditions, which effectively produce an infinite sample. This is the reason to use the far-field projection with the zero grating order filtration.

2.4 Calibration

Before heading to the photonic crystal and heterostructures simulations, we will verify the validity of such simulations by comparing the results on simple layers of different materials with results from another calculation approaches such as 4x4 Yeh formalism [15] for MOKE and Faraday effect and with analytical calculations for reflectivity.

The structure we chose is a 100 nm thick layer of Ce-substituted yttrium iron garnet (Ce:YIG) in a saturated magnetic state. Comparison of MOKE and Faraday effect calculated by FDTD with the result of Yeh's formalism is shown on picture 2.4. We can see, that the spectral trends are similar except for the spectral region between 2.8 eV - 3.2 eV of the Faraday effect. Amplitude of the curves differ, but for the purpose of this thesis, the main focus will be placed on the position of spectral peaks, which is the same for both FDTD simulation and Yeh's formalism.

There are two reasons for the difference between FDTD and Yeh's results. One is that the Faraday and MOKE are an indirect result of the FDTD simulation, because the FDTD calculates the fields, while it is a direct result of Yeh's formalism. The other reason is that the experimental data cannot be used directly in the simulation. The software automatically generates an analytical model based on the experimental data, which is then used instead. Currently the available model is only the polynomial fit, which can be modified for every material. Fits of the Ce:YIG material and yttrium iron garnet (YIG) material, which will be

used in this thesis are shown in picture 2.5 One can se several differences between polynomial parametrization and the real data. This may be the reason for the differences in the calculated Faraday and MOKE spectra.

We tried to use polynomials up to 10th order, but that leads to nonphysical maxima, such as on the real part of permittivity of YIG on figure 2.5.

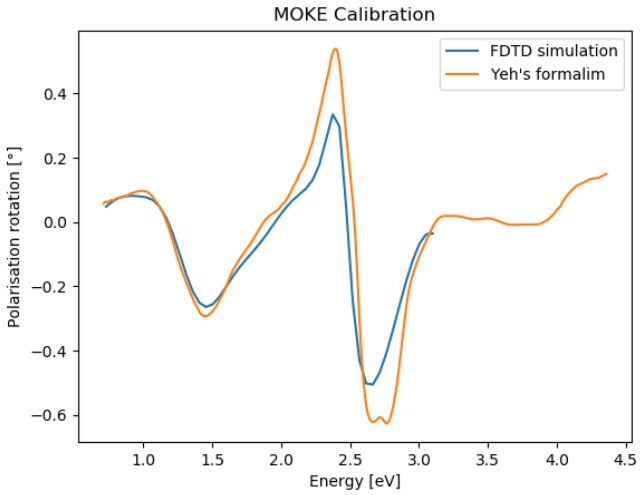

(a) Magneto-optical Kerr effect

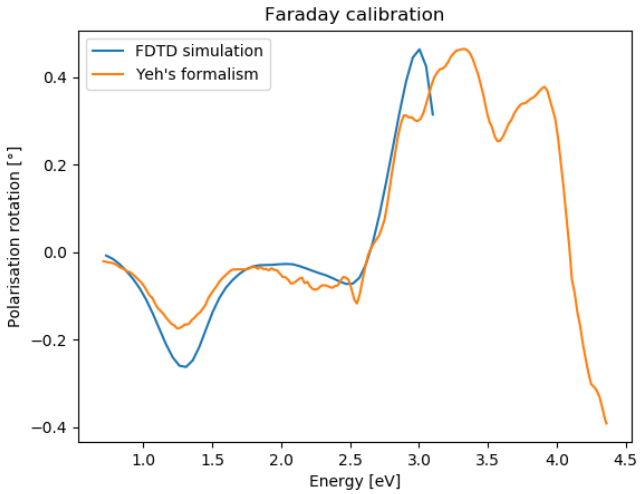

(b) Faraday effect

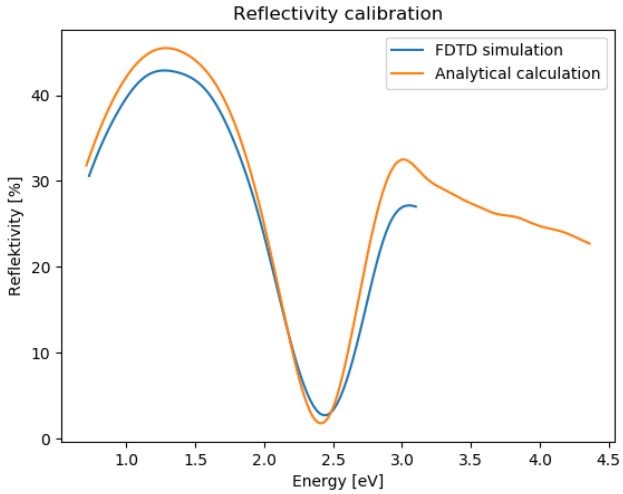

(c) Faraday effect

Figure 2.4: Comparison of magnetooptical effects calculated by FDTD simulation against results of Yeh's formalism. A simulated object is a 100 nm thick layer of Ce-substituted yttrium iron garnet in a saturated magnetic region.

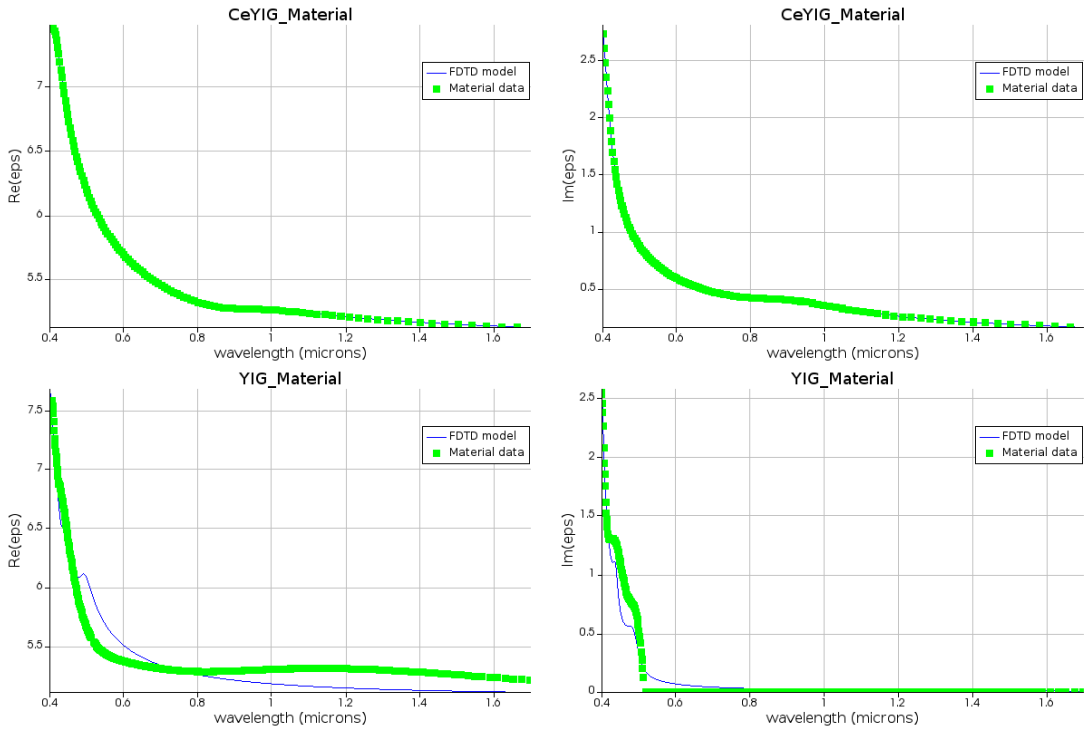

Figure 2.5: Analytical fit of the Ce:YIG and YIG material optial parameters used in the FDTD simulation.

Part II

Simulation results

3. Ce:YIG/YIG/SiO_2 Photonic crystal

We will start this chapter by simulationg a real photonic crystal that was fabricated by self-assembly method and its optical and magneto-optical response was evaluated experimentally. In doing so, we will demonstrate the limitations of the simulations together with a way to overcome some of them. Then we will have a look at how the magneto-optical response changes if we variate some of the initial parameters of the structure. We will show an interesting spectral feature in Faraday rotation spectra which we will try to maximize and tune for the usage in photonic rotators and isolators. An investigation of the origin of the spectral feature will show that such structure have a low value of transmittance for expected applications, but it will also hint towards another application - highly sensitive concentration detector. The new application is a highly sensitive concentration detector.

3.1 Real sample description

First, let us try to describe a sample of a real photonic crystal. The photonic crystal is composed of a 120 nm thick layer of Ce:YIG on another 100 nm thick layer of YIG, placed on a substrate made of SiO_2. The lattice constant a is 1000 nm and the holes are spherically-shaped in the tightest hexagonal arrangement so that the hole radius on the surface D is 690 nm for *sample 1* and 760 nm for *sample 2*. Schematic description of the structure is shown in figure 3.1. The real samples were made by self-assembly method using polystyrene spheres, which were washed out during the fabrication.

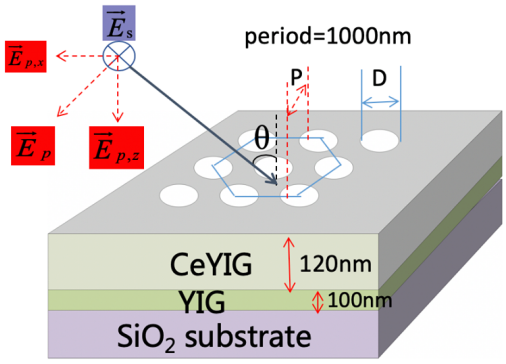

Figure 3.1: Schema of the Ce:YIG-YIG-SiO_2 photonic crystal.

This structure has two interesting properties. First, it shows a strong Faraday effect, which could be utilized in the magneto-optical isolator. And second, its Faraday rotation depends on the material, filling its holes, which could be utilized as a concentration detector.

To compare the experimental and simulated Faraday spectra, we can look at figure 3.2. There are two figures to demonstrate an angular dependence of

linear polarization of the incident wave. Observed spectral features also suggest that there are polycrystalic grains of various rotations. For example, the drop in Faraday rotation at around 2.6 eV in the experimental spectrum of the actual sample is not present in the simulation for linear polarized light light along the x-axis, but in the simulation with source polarized at 30° along the x-axis, the drop is present. Another spectral structure is around 1.6 eV, which is shifted in amplitude, but the trend is similar for both experimental and simulated data.

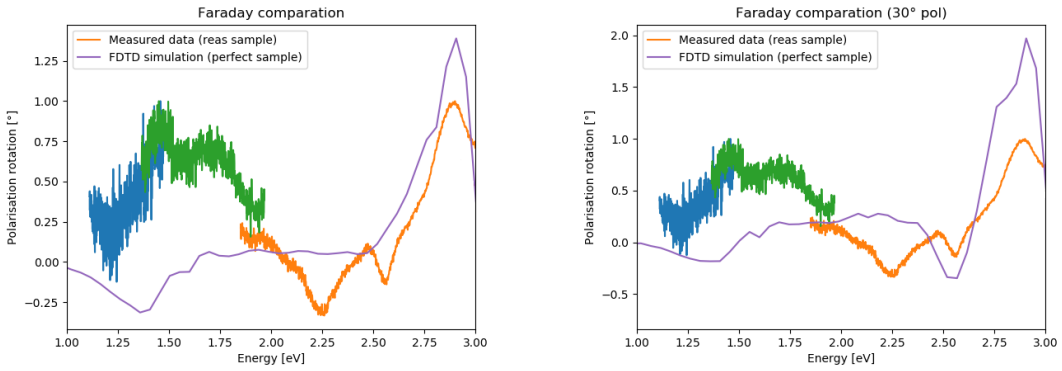

(a) (b)

Figure 3.2: Comparison of Faraday rotation of an ideal structure calculated by FDTD simulation against the measurement of a real sample. The geometry of the sample is described on figure 3.1 with value $D = 760$ nm. On the left figure (a), the incident wave is polarized in the x-axis, while on the right figure (b), it is polarised under 30in respect to the x-axis.

This sample was made by the self-assembly method of polystyrene spheres [16]. While this method is relatively cheap and suitable for larger samples, it lacks precision. In this case, the sample is efficiently not a monocrystal but rather a polycrystal with rotated grains. Another problem is that the polystyrene was not ideally removed. Lastly, there are several point defects of larger scope. These defects are captured by optical microscope in picture 3.3. The turquoise spots are areas where polystyrene was not sufficiently removed. Red lines represent the crystalographic lines and thus should be parallel. Grey dots are the bigger point defects of other kinds.

For the reasons mentioned above, the observation of lower Faraday rotation in the experimental spectra is expected. The local minimum at around 2.6 eV is due to the combination of differently rotated grains of the crystal. For our purposes, the main focus will be placed at the prominent peak position, which is the same for both the simulation and the actual sample.

3.2 Geometry optimization

Having the sample described by simulation, we can take one step further and try to optimize the structure. We aim to increase the Faraday rotation of this structure to possibly 45°. First, we will abound the self-assembly method in favor of ion etching. This change will limit the size of an actual sample but allow us to change the profile of the hole from spherical to cylindrical. Furthermore,

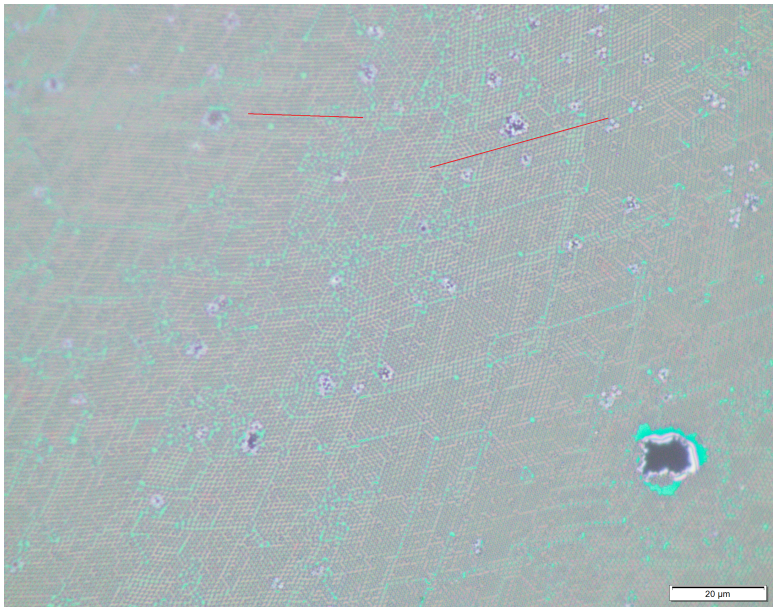

Figure 3.3: Image of a surface of a photonic crystal from figure 3.1.

the result of this method is a well-defined photonic structure, which numerical simulations can more precisely describe.

3.2.1 Ce:YIG/YIG photonic crystal

We will start the optimization process with similar design to the fabricated sample and investigate the influence of its geometrical parameters. The geometry is described in figure 3.4. The original depth hole in our previous simulations for sample 2 is:

$$h = \frac{D}{2} - \sqrt{\frac{a^2}{4} - \frac{D^2}{4}} = 175nm, \tag{3.1}$$

where a is the lattice constant, D is the hole diameter at the surface, and h is the maximum depth hole. In the following simulations we limited ourselves to cylindrical holes of the diameter D and depth h with respect to the change of the fabrication process as mentioned above.

This depth would penetrate to the YIG layer. First we focus our attention to the depth of the hole. The hole volume is increased due to the change from spherical holes to cylindrical, so the simulation was ranged from $h = 110$ nm only to $h = 170$ nm. The results of the simulation are displayed in figure 3.5.

Figure 3.5 shows a clear trend hinting towards resonant depth behavior of this photonic crystal. In order to investigate this spectral feature in Faraday rotation, other simulations were made with higher resolution around the 2.7 eV and with a smaller depth step (figure 3.6).

This resonance behavior seems promising, but it is a narrow spectral feature. To check if this is not a numerical error, another calculation was done using a Rigorous coupled-wave analysis (RCWA), a frequency-based method. It also uses raw material data in comparison to FDTD, which operates with polynomial data fits. Results from both simulation methods are shown in figure 3.7.

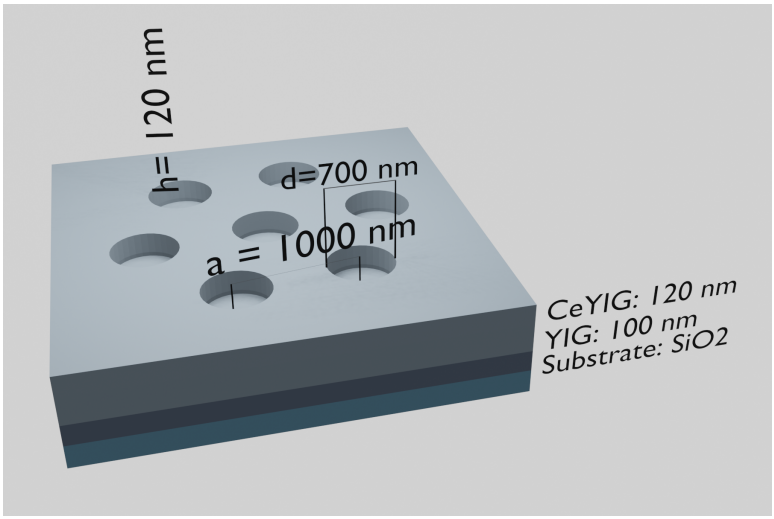

Figure 3.4: Initial design of the photonic crystal.

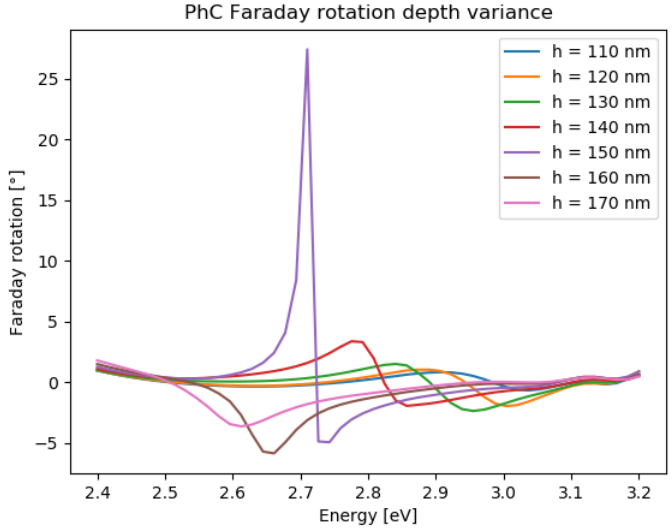

Figure 3.5: Faraday rotation spectra of photonic crystal. Geometry of the photonic crystal is described in figure 3.4.

Figure 3.7 shows that both methods predict the existence of resonant depth behavior in this hexagonal structure. However, the spectral maxima are shifted by 86 meV. This shift is caused by the difference between material data in both methods. Especially for the case of YIG the material data differ in this spectral region as can be seen from figure 2.5. This could be eliminated by improving the material data fit in the FDTD method. The improvement is not currently possible because the software supports polynomial fits only. Although tho these methods do not agree on the position of these features, it is more important that both methods confirm their existence for the same hole depth range. In reality, the peak position will depend on the fabrication quality of the sample.

Before we proceed to investigate this spectral further, we have to define a variable that we are trying to maximize. In our case, it is a figure of merit (FoM) that quantifies the quality of the device based on its faraday rotation and its

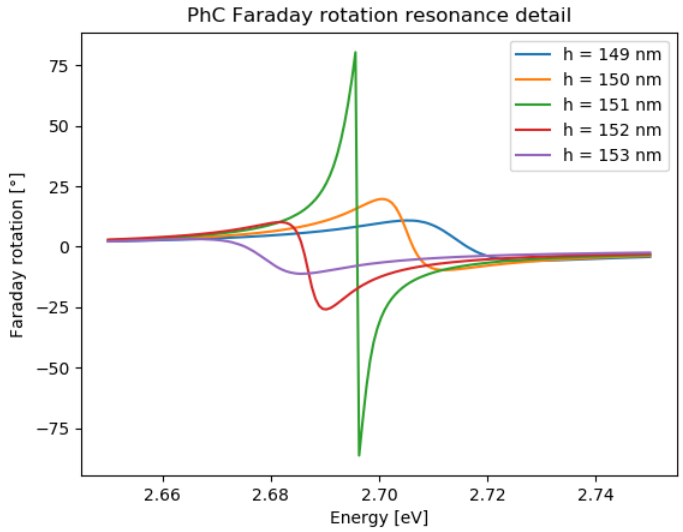

Figure 3.6: Detail of Faraday rotation spectra of photonic crystal. Geometry of the photonic crystal is described in figure 3.4.

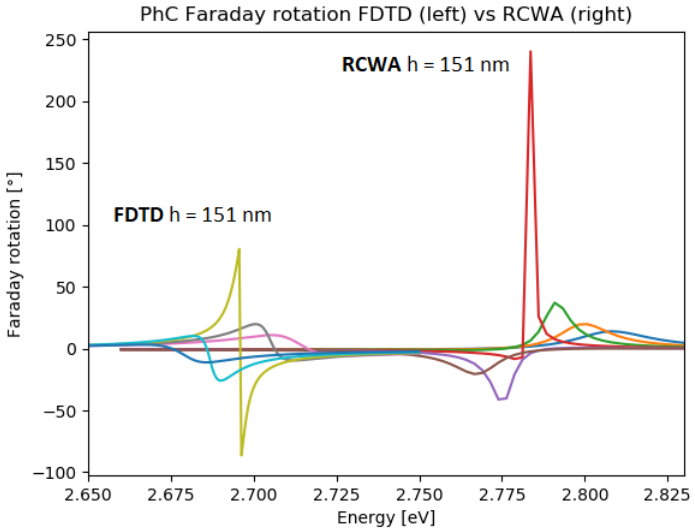

Figure 3.7: Fadaray rotation of hexagonal photonic crystal. Spectral features on the left are calculated by the FDTD method. Spectral features on right are calculated by the RCWA.

transmission according to the following equation [17]:

$$FoM \equiv \frac{\theta_f(deg/cm)}{\alpha(db/cm)} = -\frac{\theta_f(deg)}{4.34 \cdot ln(T)}, \tag{3.2}$$

where α is an absorption coefficient defined as:

$$T = e^{-\alpha t}, \tag{3.3}$$

where t is the thickness of the sample. T is its transmission, and θ_f is its Faraday rotation.

This means that if we want to maximize the figure of merit, we need to maximize the faraday rotation of the sample while keeping a high level of transmission.

Hole radius, lattice constant, and hole depth were systematically varied. Figure 3.9 shows the maximum FoM of each particular geometry. A colored dot there represents each simulation. The dot color represents the FoM value, and the position of the dot represents its geometry setting.

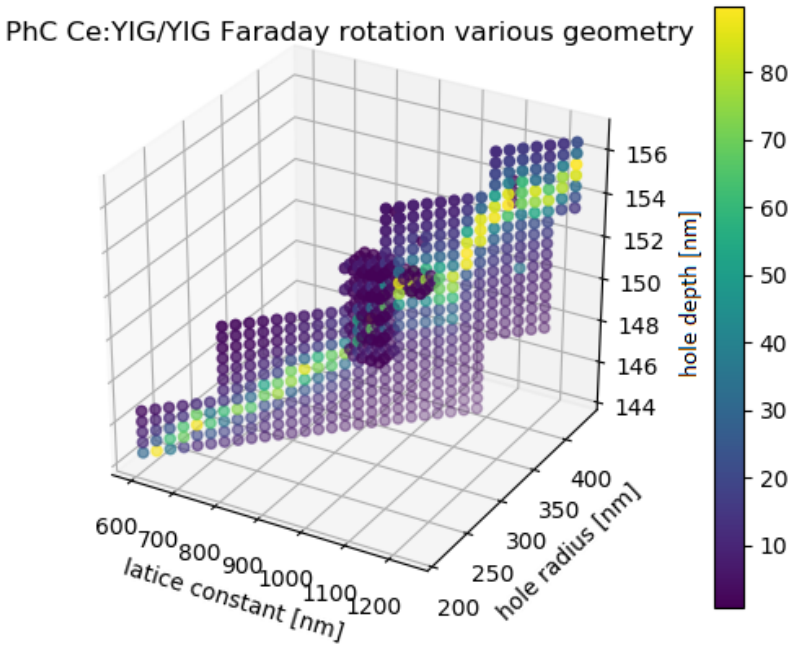

Figure 3.8: Geometry variation of hexagonal photnic crystal made of Ce:YIG and YIG layers. Coloured scale represents the maximum of the Faraday rotation of the particular geometry.

Figure 3.8 shows that there is a trend of resonant behavior for various geometry settings. The value of these FoM maxima is not exact because each geometry setting requires delicate depth tuning, while this is only a rough geometry scan of change of geometry configuration. The existence of such a trend suggests that the spectral feature can be tuned for specific applications such as for optical rotators on various wavelengths. The spectral dependence of these features is shown in figure 3.9

Figure 3.9 shows that the investigated spectral feature shifts based on the geometry configuration. For lattice constant ranging from 600 nm to 1200 nm and its other corresponding parameters required to reach theresonance, we managed to reach the desired 45° Faraday rotation between 2.64 eV and 2.83 eV. These ranges are not final. From figure 3.8, it is clear that this trend continues beyond the investigated geometry configuration. It is not a topic of this thesis to investigate the whole resonant region as increasing the calculated structure size becomes computationally demanding, and so it would be difficult to proceed with this method. However, the current trend shows that simulations with larger crystal lattice yield resonant features placed on higher energy.

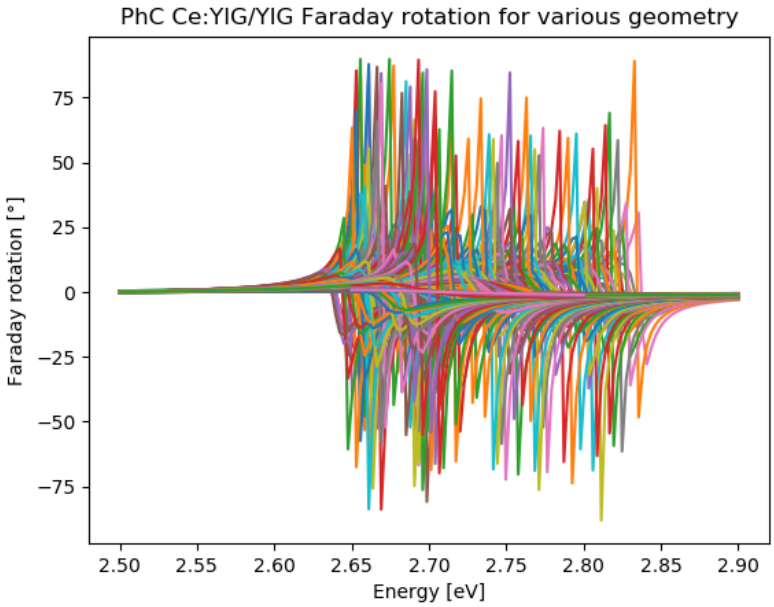

Figure 3.9: Faraday rotation of Ce:YIG and YIG photonic crystal in various geometry configuration used in figure 3.8. The purpose of this figure is to demonstrate the spectral dependency of the resonant features. Simulations with a larger lattice constant produce resonant features at higher energies.

The following figure 3.10 shows the resonant area more clearly. Simulations show that resonant behavior can be expected only while lattice constant and hole radius are changing simultaneously. (Or at least no other resonant area was found). With every 20 nm increase in lattice constant, there has to be a 7 nm increase in hole radius. Than the resonant depth can be found. The depth dependency does not seem to be analytical.

3.2.2 Ce:YIG/Bi:YIG photonic crystal

In this section, the YIG mid-layer was exchanged for the Bismut doped YIG (Bi:YIG). This middle layer can not be chosen independently. It serves as a transition material with a lattice constant similar to the Ce:YIG. (On YIG with the lattice constant of 12.51 ± 0.03 Å the layer of Ce:YIG grows with the lattice constant of 12.53 ± 0.04 Å [18]) These values are only demonstrative, an actual value of lattice constant of materials in multilayer depends on the thickness of individual layers. For this reason, only a narrow range of materials can be used.

Since the Bi:YIG has a similar lattice constant as a YIG, it can be used as its substituent. The magneto-optical activity should in comparison to YIG enhanced. We did not start with this material in the first place because we did not consider any interesting behavior for holes deeper than is the thickness of the top Ce:YIG layer, which should have worked as the primary source of the magneto-optical effect. Resonant features similar to the one in the previous section were found. Once again, there is a resonant trend behavior for various geometry settings. This trend is displayed in figure 3.11

Figure 3.12 shows that in this case, Faraday rotation of 45° or higher was

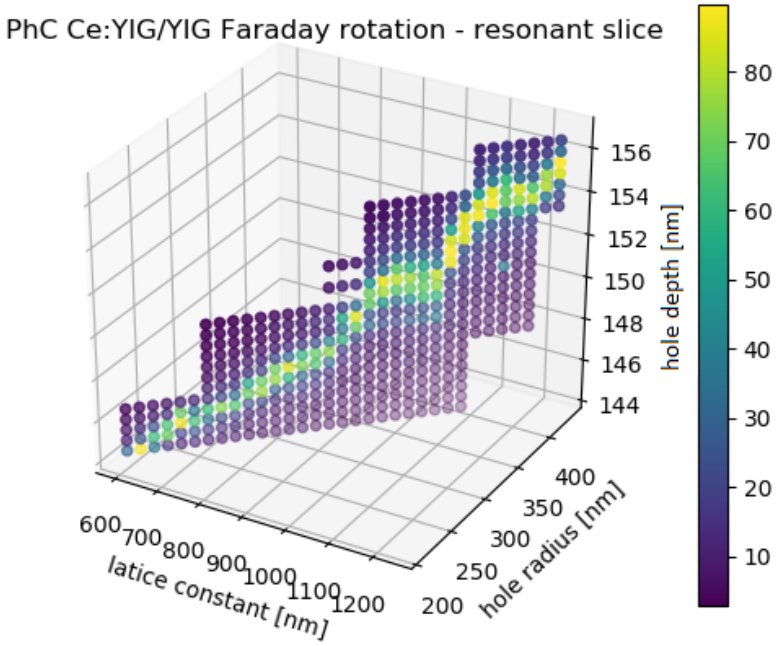

Figure 3.10: Geometry variation of hexagonal photnic crystal made of Ce:YIG and YIG layers. Coloured scale represents the maximum of the Faraday rotation of the particular geometry. Only resonant slice being shown.

reached within the spectral region of 2.63 eV and 2.86 eV for structures with lattice constant in the range between 600 nm and 1200 nm. This is only a slight increase in comparison to the YIG mid-layer in terms of spectral region range. Keep in mind that the real position of these peaks can be shifted by about 0.1 eV due to the material data fit, but at least we get the general picture about the behavior of these features and the spectral dependency.

The uneven density of resonant structures on figure 3.9 is due to the uneven distribution of examined geometry setups in the grid on figure 3.11. The reason behind this unevenity is that at first, there were 5x5x5 simulation geometry variations with the central point at first found resonant setup of a=1000 nm, d = 700 nm, and h = 151 nm. Other simulations were made with a 1% difference in these original parameters. After that, several other regions were investigated, and finally, the trend was found and confirmed by the diagonal plane simulation region with a finer depth step.

3.2.3 Transmision

At regular thin layers, the important parameter for FoM is the Faraday rotation per thickness. It is generally beneficial to maximize the Faraday rotation of the layer to reach values over 90°. The layer can then be thinned down, resulting in reaching the desired value of Faraday rotation and increasing transmissivity. In this case, the thickness of each layer is defined so that a resonant behavior would be invoked. This means that the thickness is fixed, and so we only work with

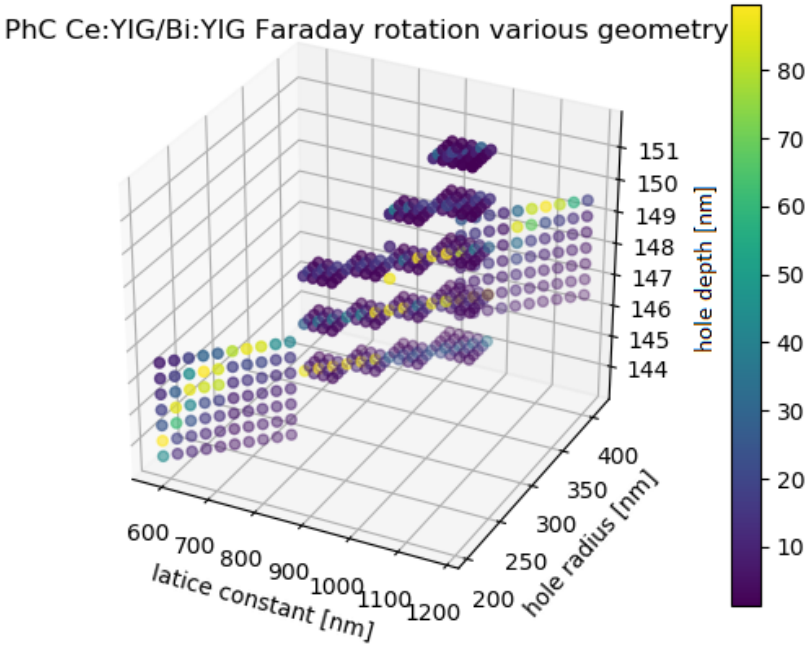

Figure 3.11: Geometry variation of hexagonal photnic crystal made of Ce:YIG, Bi:YIG layers. Coloured scale represents the maximum of the Faraday rotation of the particular geometry.

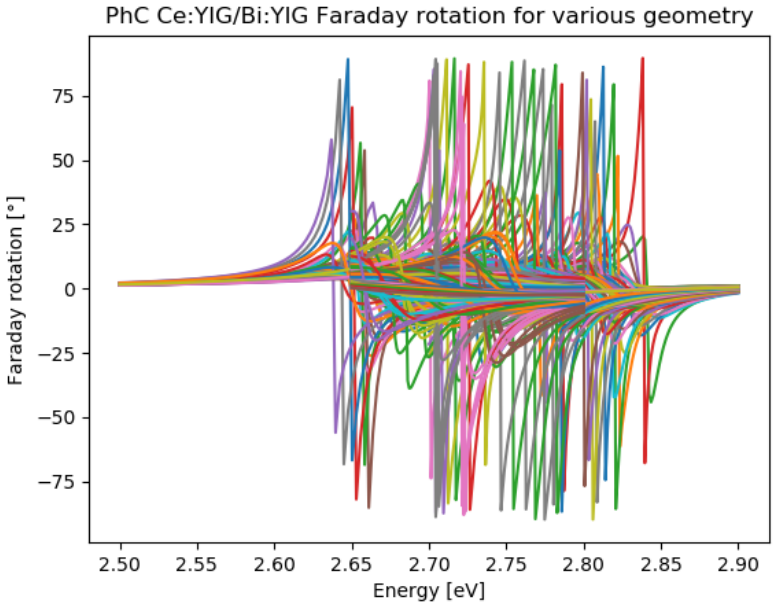

Figure 3.12: Faraday rotation of Ce:YIG, Bi:YIG photonic crystal in various geometry configuration used in figure 3.11. The purpose of this figure is to demonstrate the spectral dependency of the resonant features. Simulations with a larger lattice constant produce resonant features at lower energies.

a Faraday rotation of the whole structure. The FoM is defined as 3.2. It seems that it is always possible to reach a Faraday rotation of 90° for a certain hole depth. Thus the only other parameter we can focus on to improve the FoM is a transmission of the structure.

The comparison of the transmission of the PhC discussed in this chapter is displayed in figure 3.13. The only transmission of spectral features that reaches the value of Faraday rotation of 45° or above is being shown.

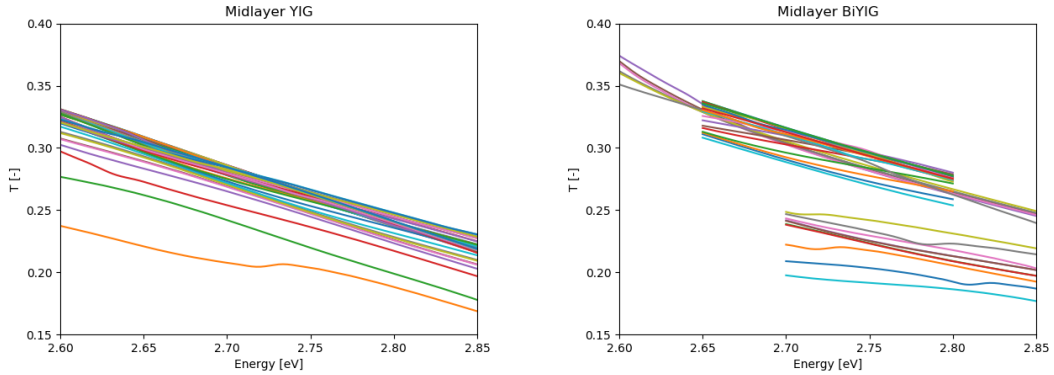

(a) (b)

Figure 3.13: Transmission of spectral features that reaches the value of Faraday rotation of 45° or above. Each line represents a photonic crystal in particular geometry configuration displayed in the figure 3.8 and 3.11. In left, we have a SiO_2-YIG-Ce:YIG photonic crystal (a) while on right there is a SiO_2-Bi:YIG-Ce:YIG photonic crystal (b).

From figure 3.13 it seems that the transmission is slightly larger while using Bi:YIG material as a mid-layer material. The discontinuity of lines in the right picture is caused by simulating only a narrow spectral region around resonant features to increase accuracy.

To confirm that Bi:YIG is a better material for maximizing FoM, we have to look at transmission in maxima of resonant features. This is done in figure 3.14

Figure 3.14 now clearly shows that using Bi:YIG as a mid-layer material leads to an increase in figure of merit. The discontinuity in Bi:YIG simulation between 2.66 eV and 2.7 eV is caused by a lower density of simulations in the sense of geometry configurations. Only resonant features with Faraday rotation of 45° and above were used. There would be more data if we would make the depth step more delicate during the geometry optimization step. For the demonstration of individual parameters, this dataset is sufficient.

As we can see, for both materials, resonances at higher energy lead to a dramatic drop in transmittance. For this reason, it is inefficient to keep investigating the geometrical arrangements that lead to these resonances at higher energy. These are the configurations with the smaller lattice parameter. The relation between resonant feature position in the spectrum and lattice parameter of the photonic crystal is displayed in figure 3.15.

The trend observed in 3.15 seems to be linear and the same for both mid-layer

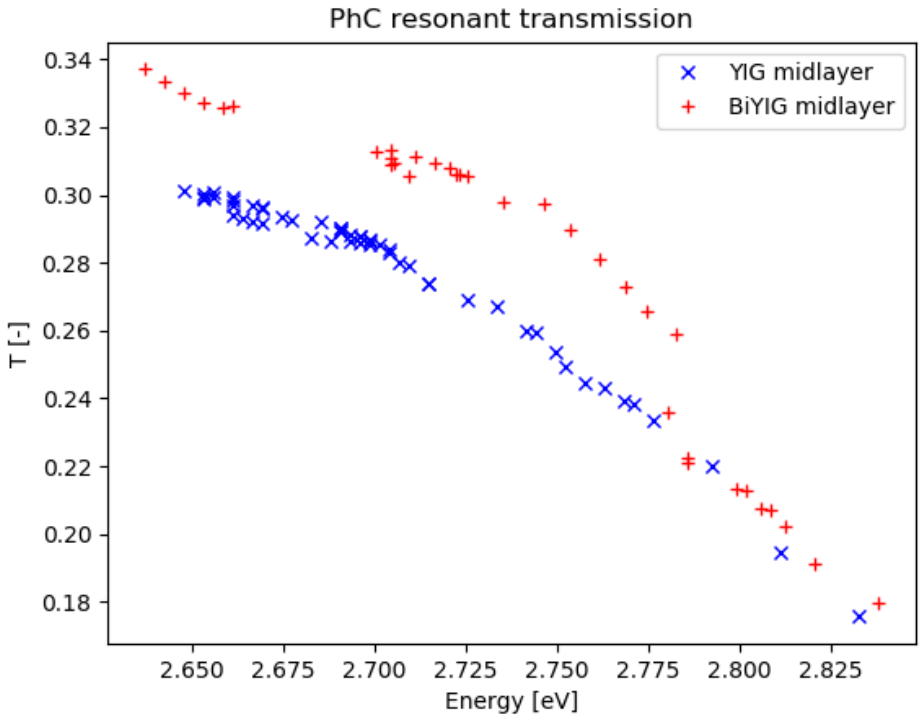

Figure 3.14: Integral Transmission of hexagonal photonic crystals in a maximum of their Faraday rotation. Blue markers represent SiO_2-YIG-Ce:YIG photonic crystal while red markers represent SiO_2-Bi:YIG-Ce:YIG photonic crystal.

materials. For YIG mid-layer variant, we obtain:

$$E[eV] = -0.0003\, a\,[nm] + 3.0351, \tag{3.4}$$

with $R^2 = 0.988$ and for Bi:YIG variant:

$$E[eV] = -0.0003\, a\,[nm] + 3.0158, \tag{3.5}$$

with $R^2 = 0.9592$.

3.2.4 Layer thickness

Since we managed to reach a sufficient value of Faraday resonance for almost every value of lattice parameter and the only thing limiting the value of the FoM is the transmittance of the structure, we should look at the thicknesses of used layers.

For this reason, we provide three additional sets of simulations. Each of these sets uses a geometrical configuration of lattice constant $a = 1000$ nm, hole radius $r = 350$ nm, and hole depth change to reach the resonant behavior. YIG is used as a mid-layer material. In the first set of simulations, the thickness of the YIG is reduced from 120 nm to 100 nm, and the thickness of Ce:YIG remains 100 nm. The maximum of the Faraday rotation is reached for the depth of 141 nm, and the resonant peak is at 2.78 eV. In the second one, the thickness of the YIG layer is also reduced to 100 nm, but now, the thickness of the Ce:YIG layer is

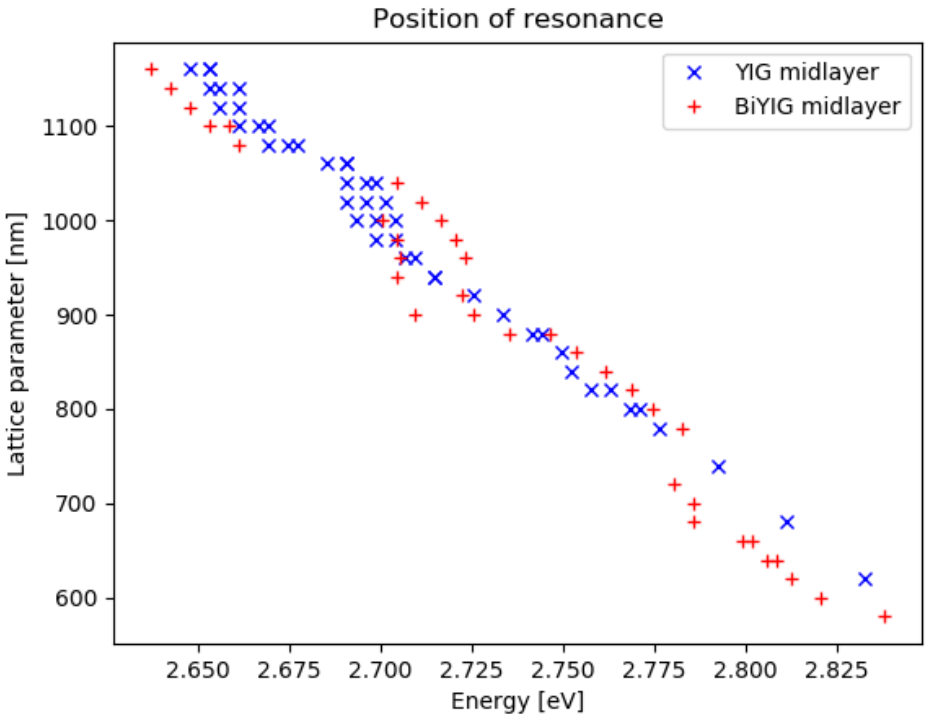

Figure 3.15: Dependence of position of Faraday rotation resonance on lattice parameter a in Ce:YIG/YIG/SiO_2 and Ce:YIG/Bi:YIG/SiO_2 photonic crystal.

also reduced, from 100 nm to 80 nm. The maximum of the Faraday rotation is reached for the depth of 135.5 nm, and the maximum of resonance is at 2.86 eV. In the third simulation set, the thickness of Ce:YIG stays at 100 nm, but the thickness of the YIG layer is reduced even further to 80 nm. The maximum of the Faraday rotation is reached for the depth of 135 nm, and the maximum of resonance is at 2.84 eV. The resulting Faraday rotation spectra are displayed in figure 3.16. Integral transmition of these designs with comparation to the original design 3.1 is displayed on figure 3.17.

3.3 Resonant field profile

Reaching the values of the figure of merit as high as 18.5 seems almost suspicious. To confirm this, we have to look at the near field inside the photonic crystal to see what causes the resonance.

The source in this simulation is an x-polarised pulse, traveling in the z-direction. To see the origin of the rotation, we have to look at the y-component of the field.

The following series of figures is comparison of the field profile of a resonant structure (figure 3.19 - 3.21) and non resonant structure (figure 3.22 - 3.24). Visualized fields are the values of at particular frequency, integrated over the time of the simulation. The frequencies are chosen so that the energy corresponds to the energy smaller then then the position of the resonance, energy of the resonance position, and energy higher than the resonance position.

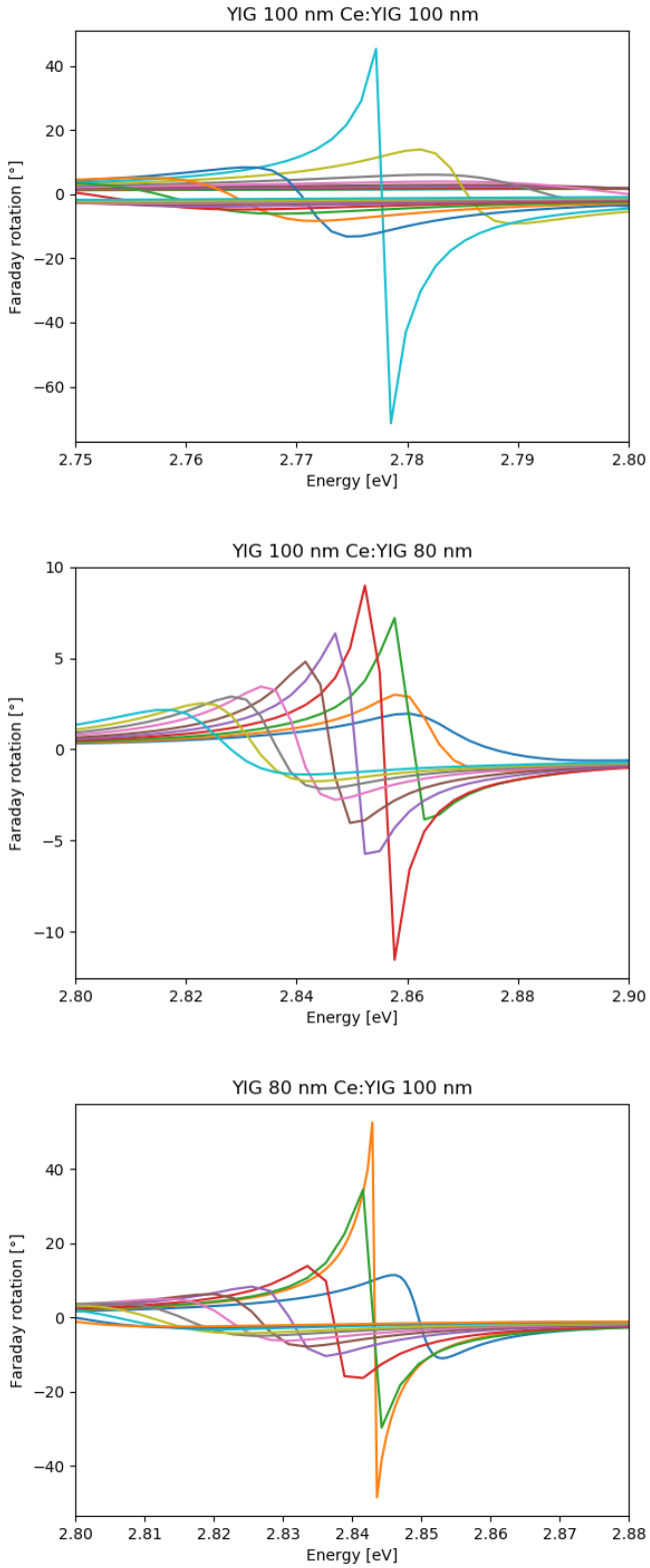

Figure 3.16: Resonant Faraday rotation of SiO_2-YIG-Ce:YIG photonic crystal with the lattice constant 1000 nm and hole radius 350 nm. The thickness of the layers used is written on top of each figure. Depth of holes varies so that resonant behaviour is reached.

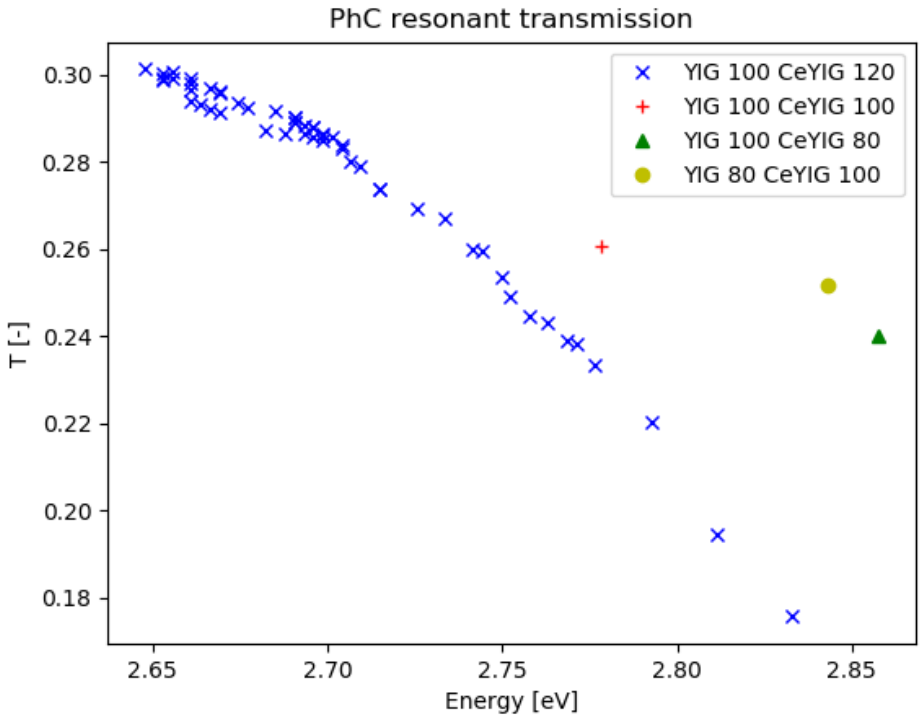

Figure 3.17: Integral transmission in the maximum of the resonance. For few simulations, the initial layer thickness was changed to show that the resonance can be found at other thicknesses and that the integral transmission can be improved.

Looking at the figure 3.18, we can see that there is actually a 180° shift in the polarization which occurs around the resonance. This shift should cause a visible difference between figures 3.21 and 3.24.

As we can see, the figure set for the resonant structure is almost identical, without any sign of a dramatic change observed in the faraday rotation.

After a detailed investigation, we found the reason behind this problem. Initially, we tested whether the position of the transmission detector would change the transmissivity, which we found out that it would not. But since we use periodic conditions in x and y direction, the simulated structure is effectively infinite, and so no matter how far the detector is, there will always be a contribution to the transmission from all diffractions orders.

The figure 3.25 shows that the transmission into 0-diffraction order is around 0.1%. This means that the figure of merit does not reach values of 18.5, but rather 2.3.

The deficient transmission is a reasonable explanation for the colossal rotation but a slight difference in the near field. The initially dominant x-polarized component is reduced due to the low transmission. The y-polarized component, induced by the magneto-optical effect, is being induced as the wave propagates through the material, and so it experiences minor reduction. At the output of the photonic crystal, both of these components are comparable in value and thus producing a significant Faraday effect ([5]).

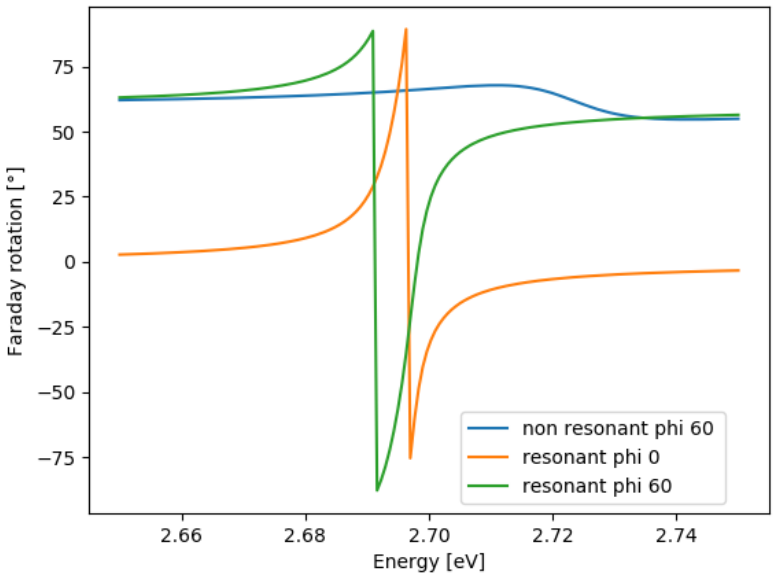

Figure 3.18: Faraday rotation of the structure described above. Notice that the green and blue lines do not start at 0°, but rather 60°. That is because the polarization angle at these simulations was set at 60°, which means that this is technically not a Faraday rotation but just the transmitted beam's polarization angle. The critical information on this figure is that the tails of the resonant lines (green and orange) are actually shifted by 180° to the other.

3.4 Concentration detector

If we look at the figures 3.20 and 3.23, which both correspond to the crosssections at the resonant energy, we can see that there is a prominent mode of light that is strongly located inside of the hole of the photonic crystal. That hints towards a significant sensitivity of such structure on the refractive index change inside the hole. Such behavior could be exploited for the construction of a concentration detector. For such a detector, the low overall transmittance is not a big issue.

For this reason, we tested the original resonant design of the photonic crystal. (120 nm thick layer of Ce:YIG on a 100 nm thick mid-layer of YIG on a SiO_2 substrate with cylindrical holes in a hexagonal arrangement that are 1000 nm apart and have 700 nm in diameter. The depth of these holes is 151 nm.) The holes were filled with a material with a refractive index, ranging from $n = 1$ to $n = 1.007$, and we calculated the faraday rotation to see whether there is some observable difference. The simulation results are depicted in figure 3.26.

The difference between individual curves in figure 3.26 is around 0.5° - 5°, depending on the curves and energy. This is a very promising sign because these values are certainly detectable.

To quantify the sensitivity of this structure, we will introduce two criteria, based on which we will select energy on which the sensitivity will be measured. The first criterium is the device's sensitivity, meaning how much does the Faraday rotation changes with the change of the refractive index inside the holes. This can be calculated simply by making a difference between the two extreme

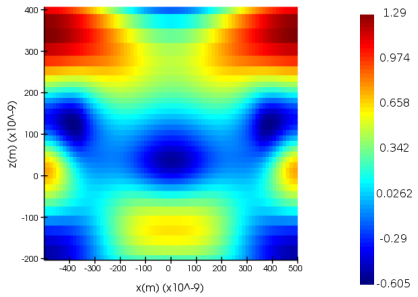

(a) Vertical slice

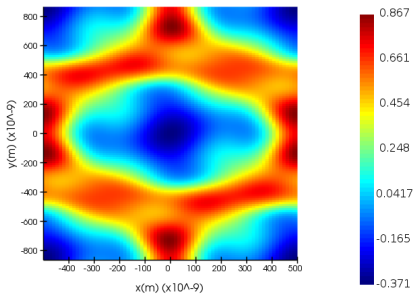

(b) Horizontal slice z = 0

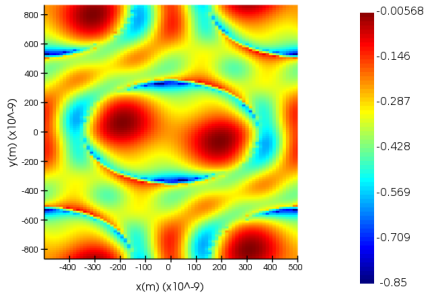

(c) Horizontal slice z = 100 nm

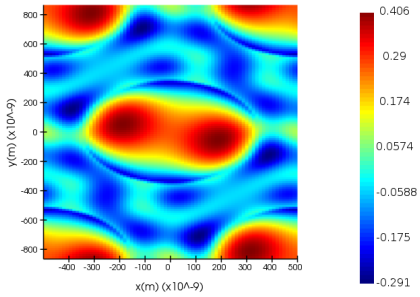

(d) Horizontal slice z = 200 nm

Figure 3.19: The profile of the y-component of the electric field inside the hole of the structure described above. The depth of the hole is 151 nm which corresponds to the resonant behavior in Faraday rotation. Subfigure (a) is a vertical slice through the middle of the hole in the x-direction. Subfigure (b) is a horizontal slice of the same field at z = 0, which is the interface between the SiO_2 substrate and the YIG. Subfigure (c) is a horizontal slice of the same field at z = 100 nm, which is the interface between the YIG and the Ce:YIG. And finally, the subfigure (d) is a slice of the same field at z = 200 nm, which is a slice in the Ce:YIG layer near the upper edge. The field profile corresponds to the 578.86 nm light or 2.142 eV.

curves, meaning $\phi_{n=1.000}(E)$ and $\phi_{n=1.007}(E)$. Energy, on which the new curve, ϕ_{dif}, reaches the maximum, would be the energy of the highest sensitivity. The second criterium is a criterium of linearity, which says how much does the Faraday rotation as a function of refractive index resembles a linear function on specific energy. It is calculated as a sum of squares of differences between an average distance of neighboring curves and its actual distance. The energy of the minimum of this function corresponds to the spectral region, where the Faraday rotation as a function of refractive index is the most linear.

Multiplying the sensitivity function $f_{sens}(E)$ with an inverted linearity function $f_{lin}(E)$ (meaning subtracting the function from its maximum), we obtain a new function $f_{score}(E)$ which works as a score to determine, which energy to use

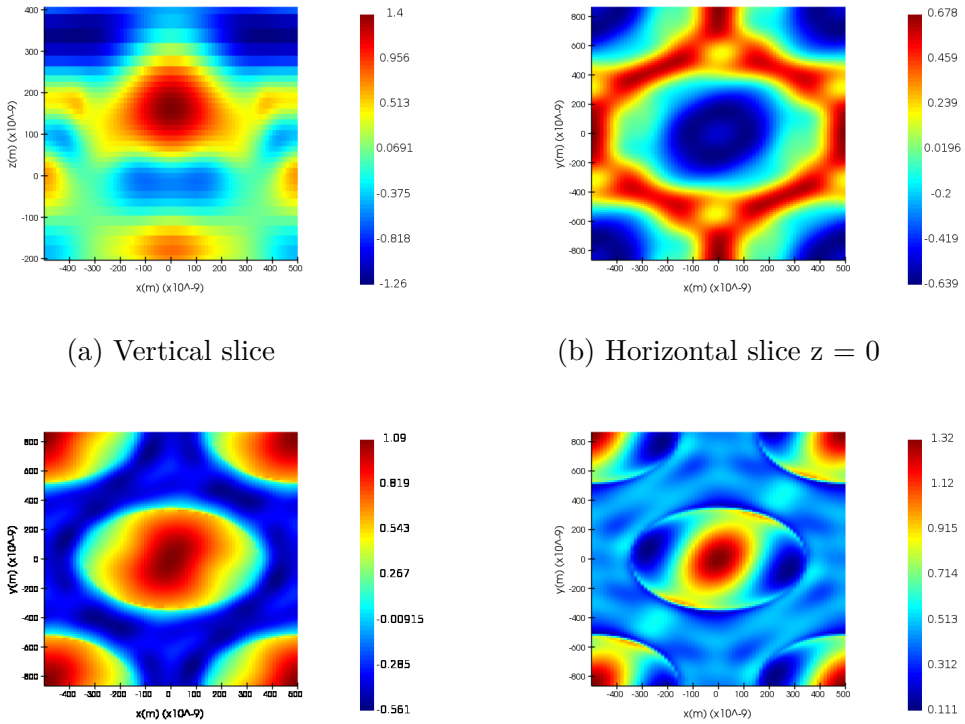

(a) Vertical slice

(b) Horizontal slice z = 0

(c) Horizontal slice z = 100 nm

(d) Horizontal slice z = 200 nm

Figure 3.20: The profile of the y-component of the electric field inside the hole of the structure described above. The depth of the hole is 151 nm which corresponds to the resonant behavior in Faraday rotation. Subfigure (a) is a vertical slice through the middle of the hole in the x-direction. Subfigure (b) is a horizontal slice of the same field at z = 0, which is the interface between the SiO_2 substrate and the YIG. Subfigure (c) is a horizontal slice of the same field at z = 100 nm, which is the interface between the YIG and the Ce:YIG. And finally, the subfigure (d) is a slice of the same field at z = 200 nm, which is a slice in the Ce:YIG layer near the upper edge. The field profile corresponds to the 459.37 nm light or 2.699 eV.

for the sensitivity definition.

$$\begin{aligned} f_{sens}(E) &= \frac{\phi_{i_{min}}(E) - \phi_{i_{max}}(E)}{i_{max} - 1} \\ f_{lin}(E) &= \sum_{i=i_{min}}^{i_{max}-1} \Big(\phi_{i+1}(E) - \phi_i(E) - f_{sens}(E)\Big)^2 \\ f_{score}(E) &= f_{sens}(E) \cdot \Big(max(f_{lin}(E)) - f_{lin}(E)\Big) \end{aligned} \tag{3.6}$$

Lower index $_i$ is indexing individual curves representing Faraday rotation of photonic crystals with different refractive index values inside its holes.

Faraday rotation as a function of the refractive index for the resonant geometry of the photonic crystal described at the beginning of this section at the maximum of the energy score function is displayed in figure 3.28. The steepness of the trend

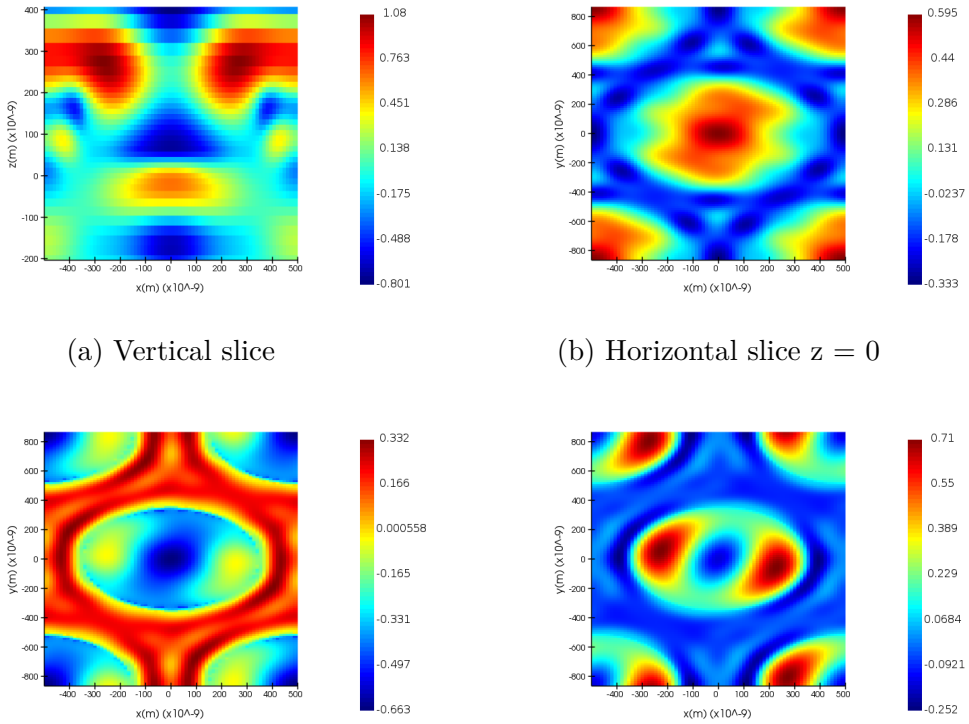

(a) Vertical slice

(b) Horizontal slice z = 0

(c) Horizontal slice z = 100 nm

(d) Horizontal slice z = 200 nm

Figure 3.21: The profile of the y-component of the electric field inside the hole of the structure described above. The depth of the hole is 151 nm which corresponds to the resonant behavior in Faraday rotation. Subfigure (a) is a vertical slice through the middle of the hole in the x-direction. Subfigure (b) is a horizontal slice of the same field at z = 0, which is the interface between the SiO_2 substrate and the YIG. Subfigure (c) is a horizontal slice of the same field at z = 100 nm, which is the interface between the YIG and the Ce:YIG. And finally, the subfigure (d) is a slice of the same field at z = 200 nm, which is a slice in the Ce:YIG layer near the upper edge. The field profile corresponds to the 411.54 nm light or 3.01 eV.

is around 2.66°/0.001n. The trend is linear only for small changes of the refractive index, but it could definitely be used in some applications. Since the resonant position is tuneable, we can assume that it could be tuned for various refractive indexes as well.

3.5 Ce:YIG/YIG/SiO_2 PhC sumarry

In conclusion, at the beginning of the chapter, we show that the FDTD method can be used to some extent to model a real photonic crystal based on garnet materials (Fig 3.2). We then optimized the initial design, which led to the discovery of resonance in Faraday rotation, reaching a total of 180° values (Fig 3.18). Based on the crystal's geometry, this spectral feature is tuneable across s specific region of the spectrum (Fig 3.10). The mid-layer YIG material was replaced with Bi:YIG, which led to an increase in transmissivity (Fig 3.14). We then made a brief test

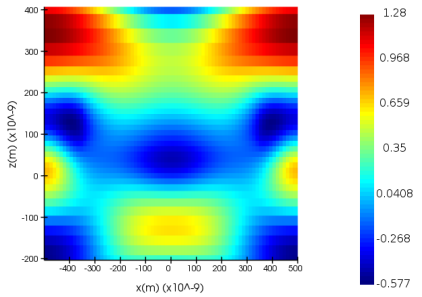

(a) Vertical slice

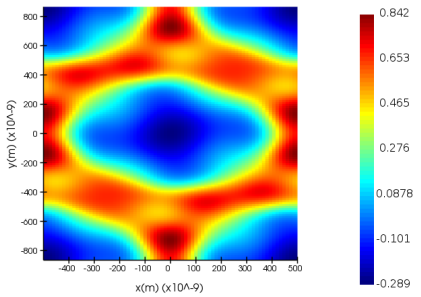

(b) Horizontal slice z = 0

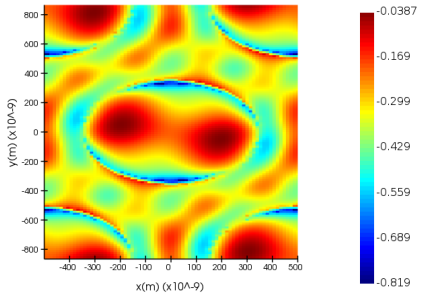

(c) Horizontal slice z = 100 nm

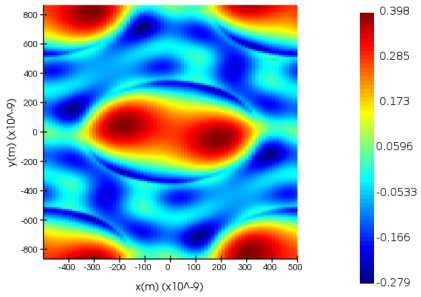

(d) Horizontal slice z = 200 nm

Figure 3.22: The profile of the y-component of the electric field inside the hole of the structure described above. The depth of the hole is 148 nm which does not correspond to the resonant behavior in Faraday rotation. Subfigure (a) is a vertical slice through the middle of the hole in the x-direction. Subfigure (b) is a horizontal slice of the same field at z = 0, which is the interface between the SiO_2 substrate and the YIG. Subfigure (c) is a horizontal slice of the same field at z = 100 nm, which is the interface between the YIG and the Ce:YIG. And finally, the subfigure (d) is a slice of the same field at z = 200 nm, which is a slice in the Ce:YIG layer near the upper edge. The field profile corresponds to the 578.86 nm light or 2.142 eV.

of whether it is possible to find the resonant spectral feature for photonic crystal with different layer thicknesses, which turned out to be successful, and it led to even better transmission (Fig 3.17). The transmission into zero diffraction order turned out to be significantly lower than we anticipated (Fig 3.25). This led to a decrease of the figure of merit defined in (Eq 3.2) from 34.5 to 4.6. Investigation of the origin of the spectral features showed potential towards the structure being highly sensitive on a change of a refractive index inside its holes (Fig 3.23). This turned out to be true. The Faraday rotation of this structure in the resonance is highly sensitive with respect to the change of the refractive index (Fig 3.26). The sensitivity reaches several degrees per thousandth of refractive index (Fig 3.28).

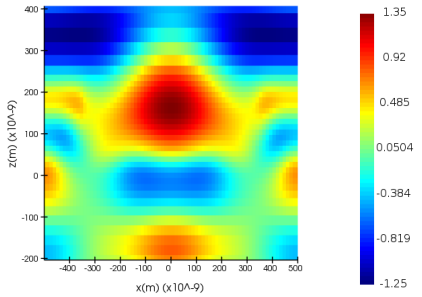

(a) Vertical slice

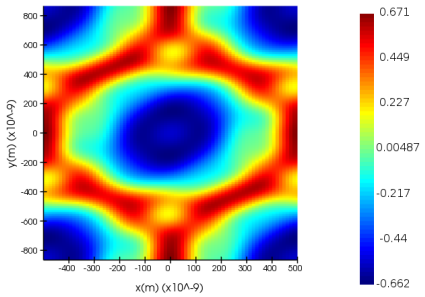

(b) Horizontal slice z = 0

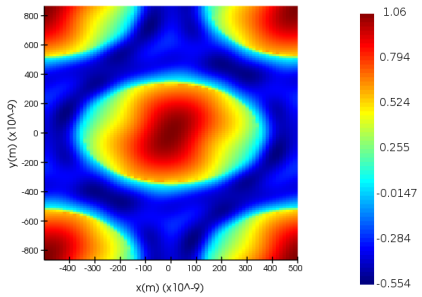

(c) Horizontal slice z = 100 nm

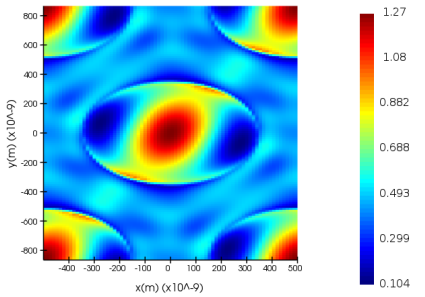

(d) Horizontal slice z = 200 nm

Figure 3.23: The profile of the y-component of the electric field inside the hole of the structure described above. The depth of the hole is 148 nm which does not correspond to the resonant behavior in Faraday rotation. Subfigure (a) is a vertical slice through the middle of the hole in the x-direction. Subfigure (b) is a horizontal slice of the same field at z = 0, which is the interface between the SiO_2 substrate and the YIG. Subfigure (c) is a horizontal slice of the same field at z = 100 nm, which is the interface between the YIG and the Ce:YIG. And finally, the subfigure (d) is a slice of the same field at z = 200 nm, which is a slice in the Ce:YIG layer near the upper edge. The field profile corresponds to the 459.37 nm light or 2.699 eV.

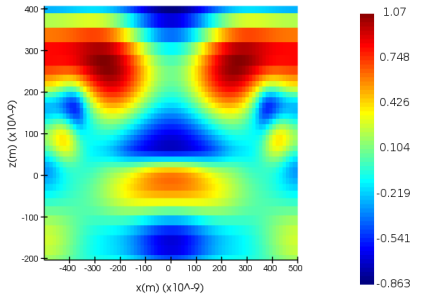

(a) Vertical slice

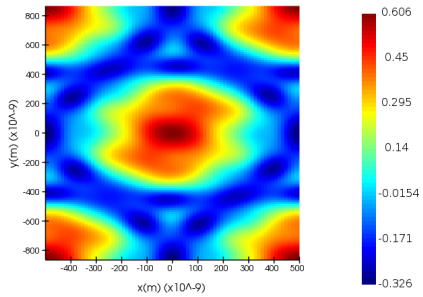

(b) Horizontal slice z = 0

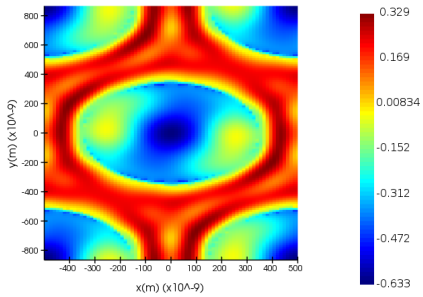

(c) Horizontal slice z = 100 nm

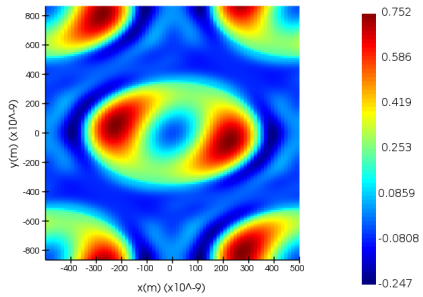

(d) Horizontal slice z = 200 nm

Figure 3.24: The profile of the y-component of the electric field inside the hole of the structure described above. The depth of the hole is 148 nm which does not correspond to the resonant behavior in Faraday rotation. Subfigure (a) is a vertical slice through the middle of the hole in the x-direction. Subfigure (b) is a horizontal slice of the same field at z = 0, which is the interface between the SiO_2 substrate and the YIG. Subfigure (c) is a horizontal slice of the same field at z = 100 nm, which is the interface between the YIG and the Ce:YIG. And finally, the subfigure (d) is a slice of the same field at z = 200 nm, which is a slice in the Ce:YIG layer near the upper edge. The field profile corresponds to the 411.54 nm light or 3.01 eV.

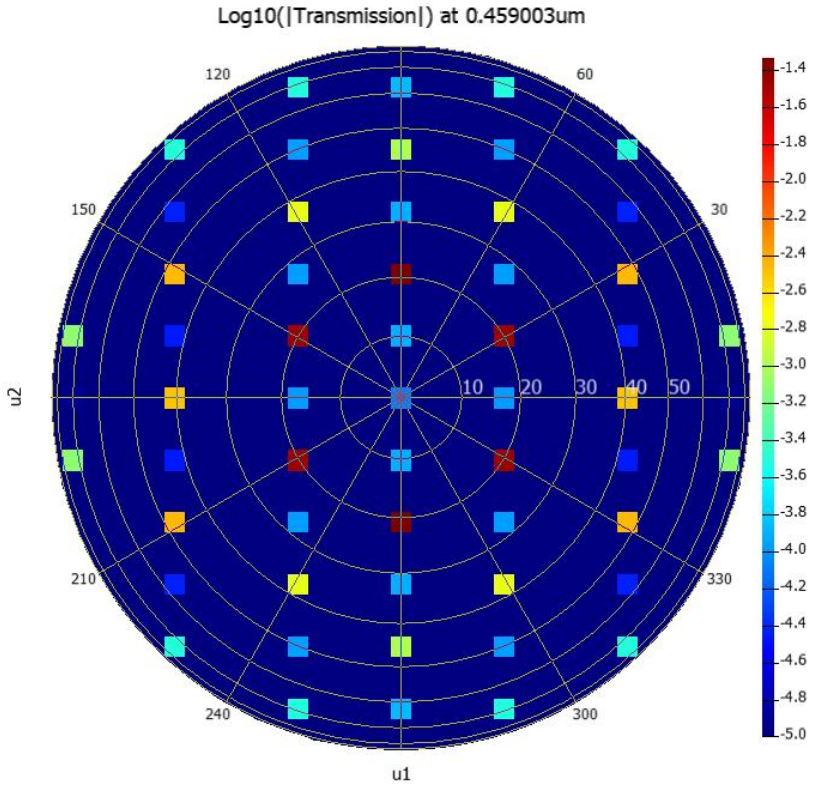

Figure 3.25: Logarithmic transmission into diffraction orders of the Ce:YIG/YIG photonic crystal in the resonant geometry settings at the resonant energy.

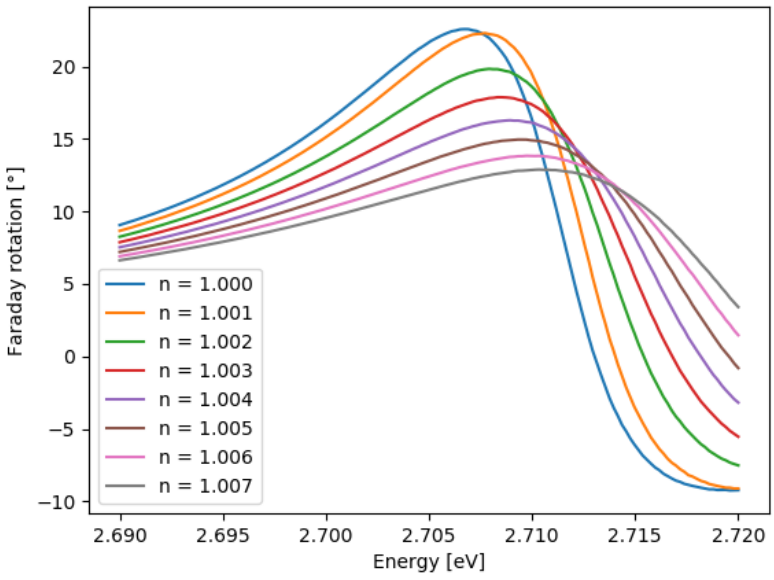

Figure 3.26: Faraday rotation of the photonic crystal described above. The refractive index n is different for each simulation.

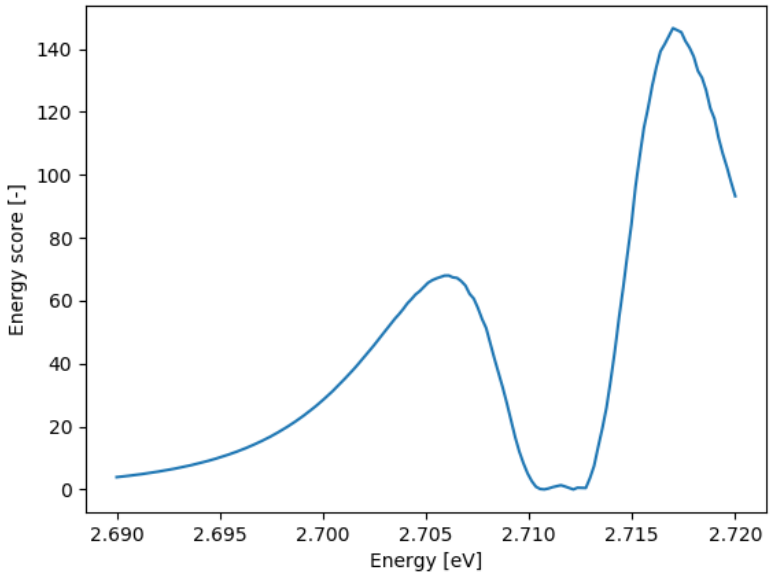

Figure 3.27: Value of energy score for photonic crystal described above as defined in equation 3.6

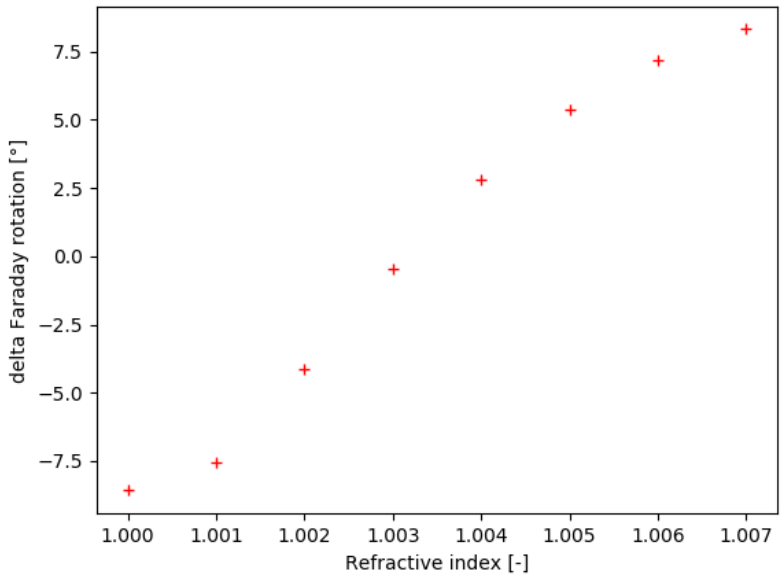

Figure 3.28: Sensitivity towards the change of the refractive index in the holes of photonic crystal described above at the energy, determined by the energy score.

4. Optically active element

An exciting property of ferromagnetic shape memory alloys, such as NiMnGa, is that the ferromagnetic domains are coupled into two crystal variants. Applying an external magnetic field leads to reordering of the crystal lattice, producing an observable deformation of the structure that, according to [19] reaches around 6-10%. A photonic crystal made out of this material would have its optical properties, such as reflectivity, sensitive to the deformation's magnitude. This means that such a device could be used as a optically active element, deformation detector or a detector of a magnetic field. In this chapter, we will try to design a device that will be sensitive towards the deformation. We will investigate three designs: a photonic crystal with cylindrical holes in a hexagonal pattern, cylindrical pillars in a square pattern, and finally, self-standing foil with cylindrical holes in a square pattern.

4.1 Hexagonal hole pattern

The first idea was to use a concept similar to the one in the previous chapter, a hexagonal photonic crystal on a substrate. In this case, the photonic crystal is made out of a 50 nm thick layer of Co:NiMnGa on a 20 nm mid-layer of chromium, which stands on a substrate made out of magnesium oxide. Into the top layer, a hexagonal pattern of a cylindrical hole is fabricated (see figure 4.1).

The property of interest will be the reflectivity of this structure. The mid-layer is included purely for practical reasons because it is easier to grow a Co:NiMnGa structure on chromium than on magnesium oxide.

The optimization process itself will target the lattice constant a and the hole radius r. There will also be a third parameter, which is the deformation. The magnetic field is turned off in this case because the material will keep its shape.

We will model the material deformation by changing the hole profile from circular co elliptical while keeping the total volume of the material the same. We will do that by introducing the deformation parameter d. The hole radii can be

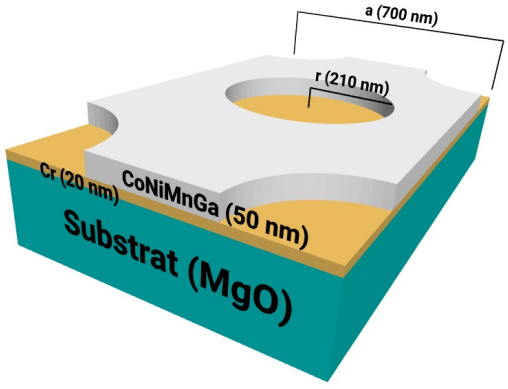

Figure 4.1: An elementary cell of the hexagonal hole pattern design of the optically active element. This cell is periodically repeated in the simulation.

described as:

$$\begin{aligned} r_1 &= r_0(1+d) \\ r_2 &= \frac{r_0}{1+d}, \end{aligned} \tag{4.1}$$

where r_1 is the size of the ellipse's major axis and r_2 is the size of the minor axis of the ellipse. We denote the hole radius parameter as r_0. Note that this assumes an ideal deformation, which occurs only in one direction and is homogenous. In reality, the material might get deformed around other axes due to the tension, it might crack, or some other form of defect could emerge.

4.1.1 Material input

Before we proceed to the simulation, let us have a look at the material data.

For the description of MgO material, we used data from **refractive index website.** The problem is that there is only refractive index data, and so we calculated the relative permittivity simply by squaring the refractive index, assuming relative permeability to be equal to one for the spectral region we are working with. The extinction coefficient is not listed, so we assume it to be zero (MgO material is not absorbent in this spectral region), making the permittivity values real. The problem is that the real and imaginary part of the permittivity is not independent but rather connected by Kramers-Kronig relations [20]. These relations require the whole spectrum to be known, which is impossible to measure, so software such as LUMERICAL imitates them to some extend by their internal models, which we have no control over. For this reason, there is a disagreement in the imaginary part of the fitted permittivity in magnesium monoxide on figure 4.2. This disagreement is not significant and since we want to simulate only reflection and the disagreement is in the bottom layer, this should not be an issue.

4.1.2 Design shortcomings

In the current model, we use an isotropic permittivity for the deformed Co:NiMnGa, but the deformation could induce an anisotropy. Another potential problem is that the layer is way too thin compared to other dimensions of the structure. This can lead to cracks in the material. Another concern is that the substrate will not allow the top layer to deform. For this reason, the other design focuses on self-standing foil.

4.1.3 First data set

In the first badge of simulations, we leave the lattice constant $a = 700$ nm fixed and vary only the hole radius and the deformation parameter. The data set contains simulations of structures with a hole radius ranging from 50 nm to 290 nm with a step of 10 nm. The deformation ranges from 0 % to 15 % with a 5 % increase.

With an increase in the radius of holes, there starts to appear a drop in reflectivity at around 2 eV, which is maximized at a hole radius of 260 nm and

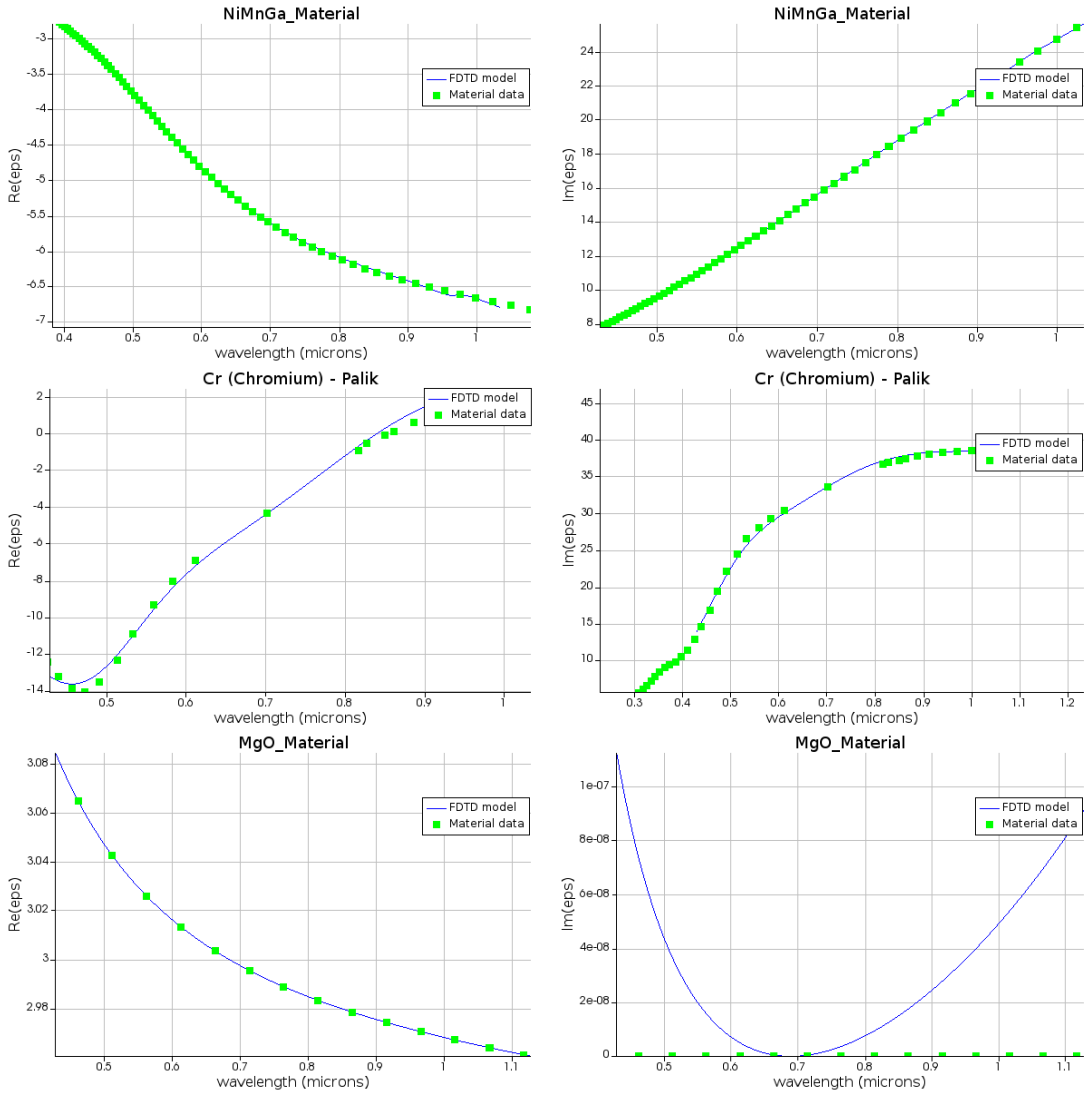

Figure 4.2: The analytical fit of the real and imaginary part of permittivity of materials used in the FDTD simulation for the optically active element design.

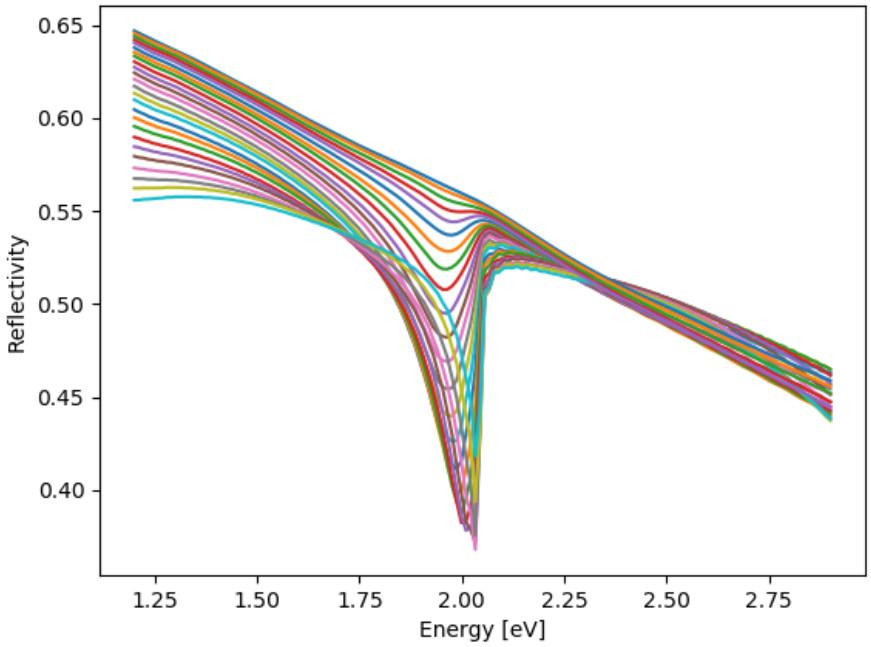

Figure 4.3: The reflectivity of the structure with various hole radiuses without a presence of deformations. At 1.25 eV, the highest curve represents the structure with a hole radius of 50 nm, and as the curve gets lower, it represents structures with a higher radius up to 300 nm. These curves are ordered at lower energies, but at around 1.7 eV, the order gets lost as the structure with the highest radius no longer yields the lowest reflectivity.

then starts to narrow and vanish. The vanishing may be caused by the delicacy of the simulation of energy spectra. See figure 4.3.

The geometry with the most significant drop in reflectivity was selected to investigate how it behaves under deformation. At this simulation resolution, the difference in reflectivity under deformation at the hole radius of 260 nm is almost unrecognizable. This might improve if the relative change under higher resolution is calculated. See figure 4.4.

The change in reflectance with increasing deformation is more significant in simulations with hole radii that produce a broader drop in reflectivity. An example is the radius of 200 nm displayed in figure 4.5.

4.1.4 Simulation under higher resolution

Once the general behavior of the structure was known, another badge of simulations was made. Using the same lattice constant and the deformation parameter as previously, but this time the hole radius ranges only from 250 to 300 nm. The most important change in a setting is the spectral region ranging only from 1.9 to 2.1 eV. This change increases the resolution of the spectrum, allowing us to investigate more delicate special features if there are any.

The detailed simulation confirms that increasing the hole radius further does not increase the drop in reflectivity. 4.6

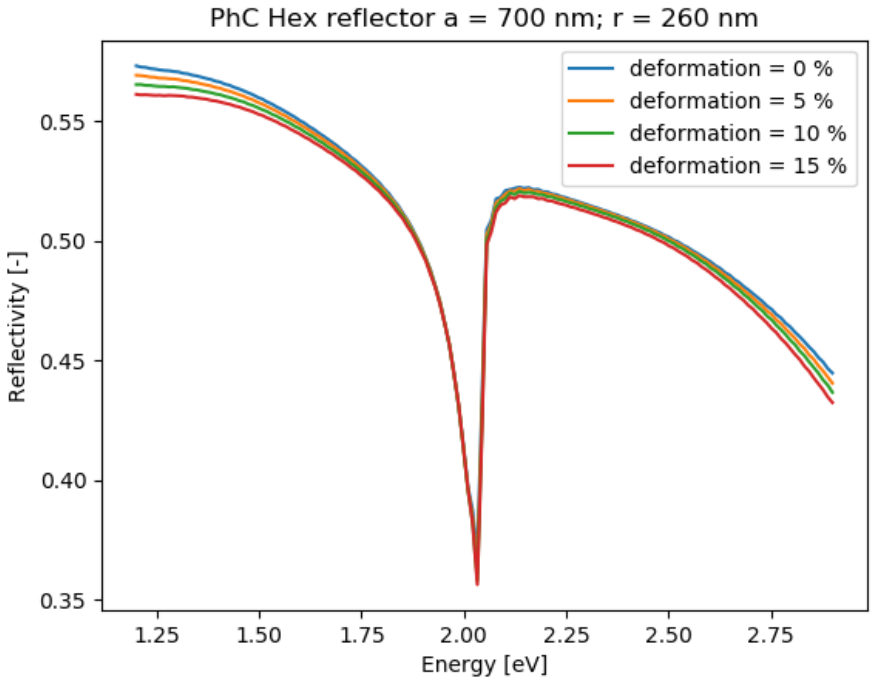

Figure 4.4: The reflectivity of the structure with a hole radius of 260 nm and four different values of the deformation parameter. This radius produces the highest drop in reflectivity.

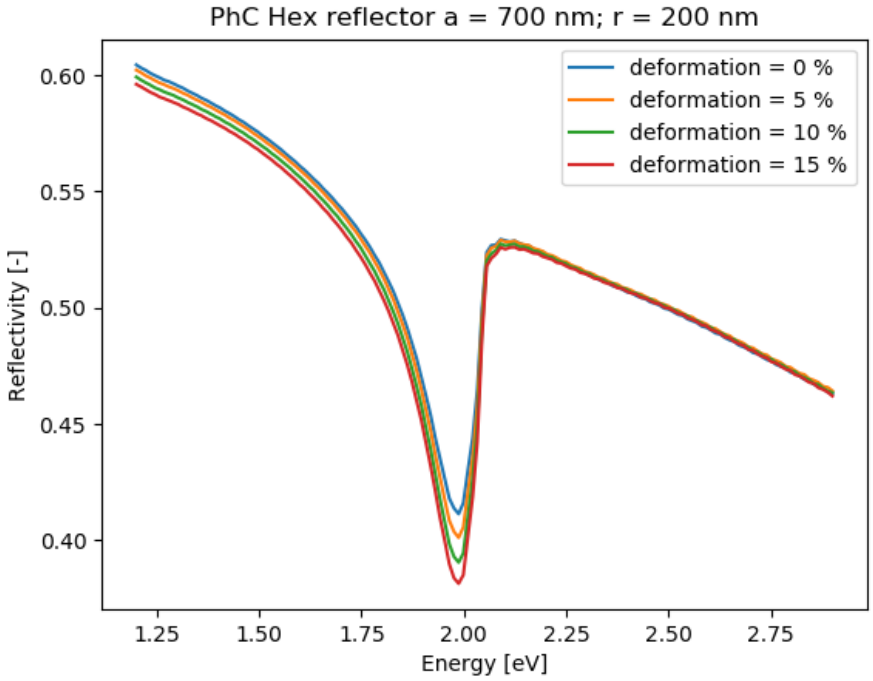

Figure 4.5: The reflectivity of the structure with a hole radius of 200 nm and four different values of the deformation parameter. In this case, the reflectivity is more sensitive towards a change in the deformation parameter.

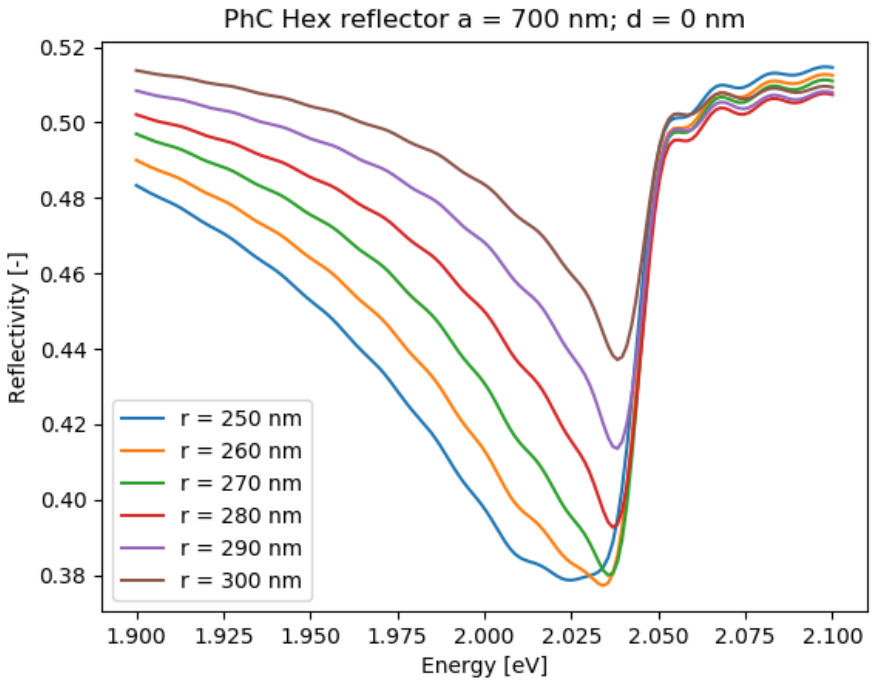

Figure 4.6: The reflectivity of the structure with various hole radiuses without a presence of deformations under higher detail.

A figure 4.7 is the detailed version of figure 4.4. It confirms that although this geometric configuration maximizes the undeformed drop in reflectivity, it does not maximize the sensitivity towards the change in deformation.

4.1.5 Optimization clasification

Before we can start optimizing the structure, we have to classify what we are going to optimize. For this purpose, we will define a sensitivity S as a parameter of a hole radius r_0:

$$S(r_0) = \left| \frac{\partial min[R_{r_0,d}(E)]}{\partial d}(d = 0.05) \right|, \tag{4.2}$$

or in other words, we take a structure with a defined hole radius r_0, we calculate the spectral reflectivity $R_{r_0,d}(E)$ for various deformation parameters d, we pick the local minimum of the reflectivity and parametrize it as a function of the deformation parameter. Then we take the absolute value of the slope, and this is the sensitivity $S(r_0)$ which demonstrates how much does the reflectivity in minimum change if we deform the sample.

The calculation of the slope around the $d = 0.05$ is justified by the figure 4.8, which shows that we could use a linear fit as well. In some simulations, the reflectivity of minimum diverses form the linear trend around the $d = 0.15$, but that is a value that we can not expect to reach anyway since the maximum observed deformation is around $d = 0.1$.

The sensitivity as a function of the hole radius is for lattice constant $a = 700$ nm shown in figure 4.9.

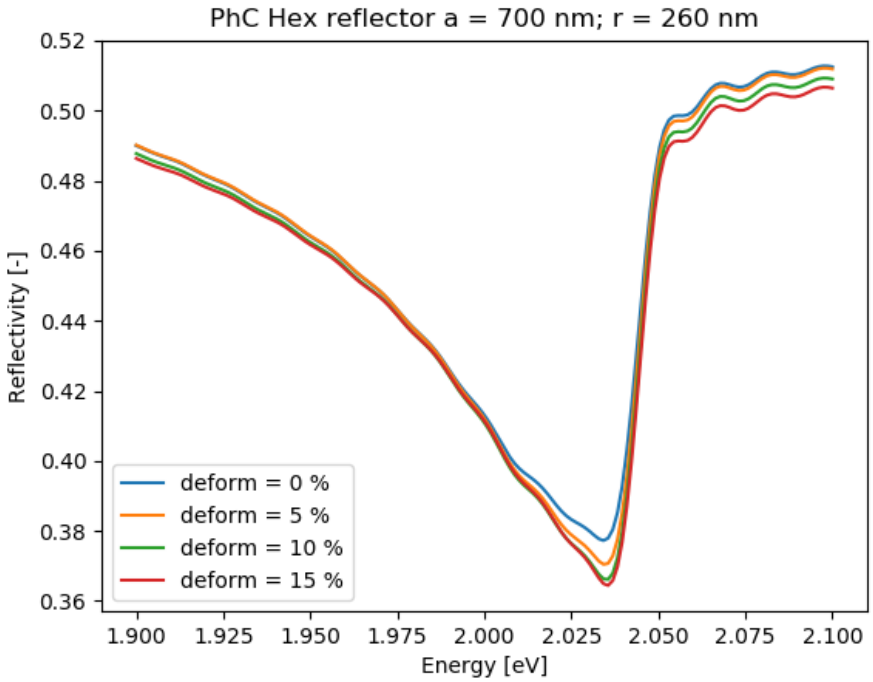

Figure 4.7: The reflectivity of the structure with a hole radius of 260 nm and four different values of the deformation parameter detailed. This radius produces the highest drop in reflectivity.

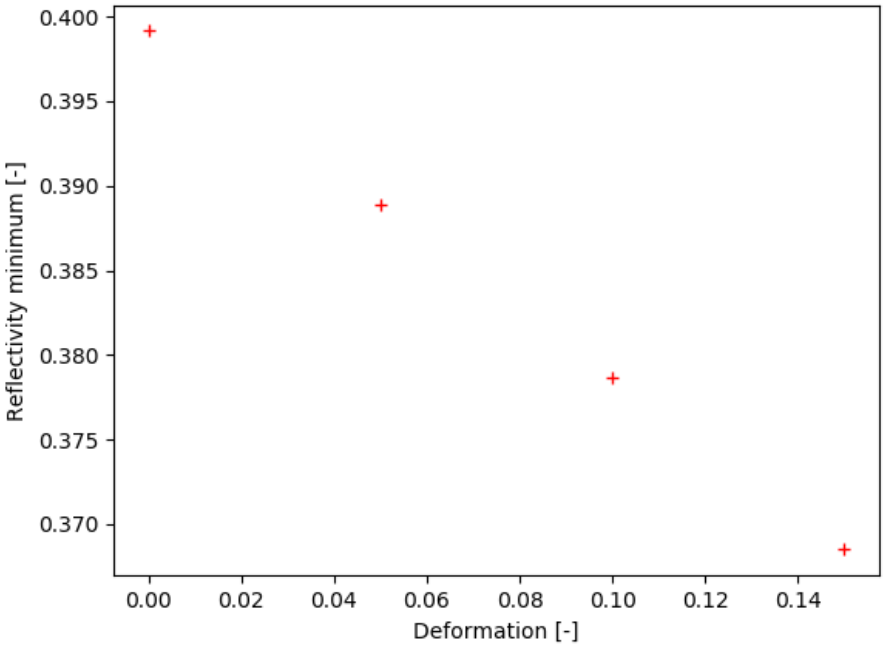

Figure 4.8: The minima of reflectivity of structure with a hole radius of 210 nm for various deformation parameters.

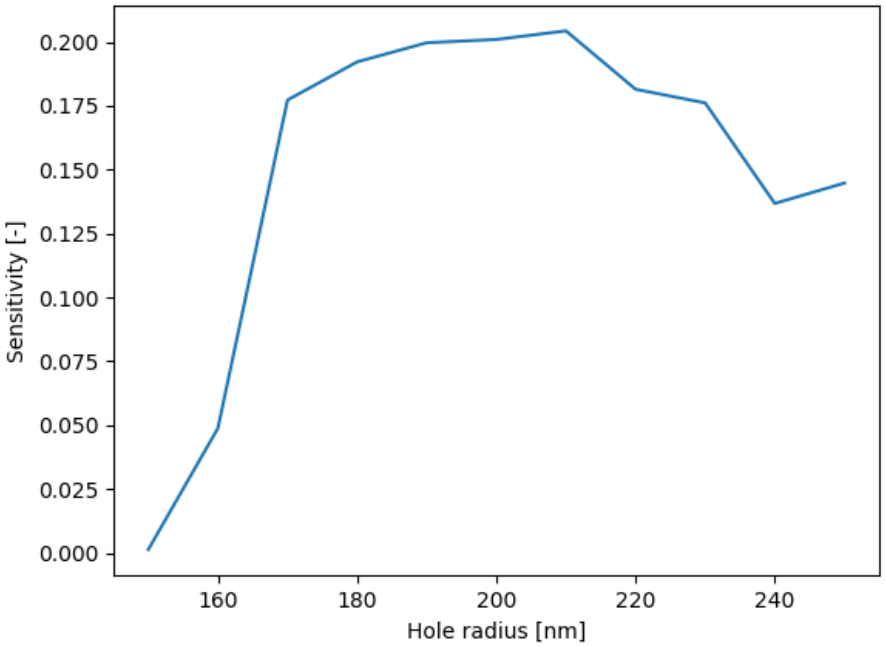

Figure 4.9: Sensitivity as a function of hole radius as defined in equation 4.2 The lattice constant $a = 700$ nm.

The figure 4.9 shows that from this data sample, the most efficient structure, with the highest value of sensitivity (4.2), is the structure with a hole radius of 210 nm.

4.2 Square pillar pattern

Another type of structure that we investigate is a 500 nm thick layer of MgO with pillars of Cr and Co:NiMnGa in square arrangement on top of it. The lattice constant is 1600 nm, and the radius of these pillars is 300 nm. The thickness of these materials is the same as in the previous design, which is 50 nm of Co:NiMnGa on top of 20 nm of Cr (see figure 4.11).

For such a structure, the transmittance was calculated. (Figure 4.12)

There looks to be potentially an interesting behavior in transmission around 0.8 eV. The problem is that the material data are not valid in this spectral region. (The fit of the material data is shown in figure 4.13). Since the laboratory equipment does not allow measuring the material data under 1 eV, this design was abounded. There is a possible way around this, which is changing the lattice constant, but other projects got a higher priority, and there was a concern about the pillars falling off due to the deformation. This is another reason to abound the design with substrate altogether and to move to the self-standing film.

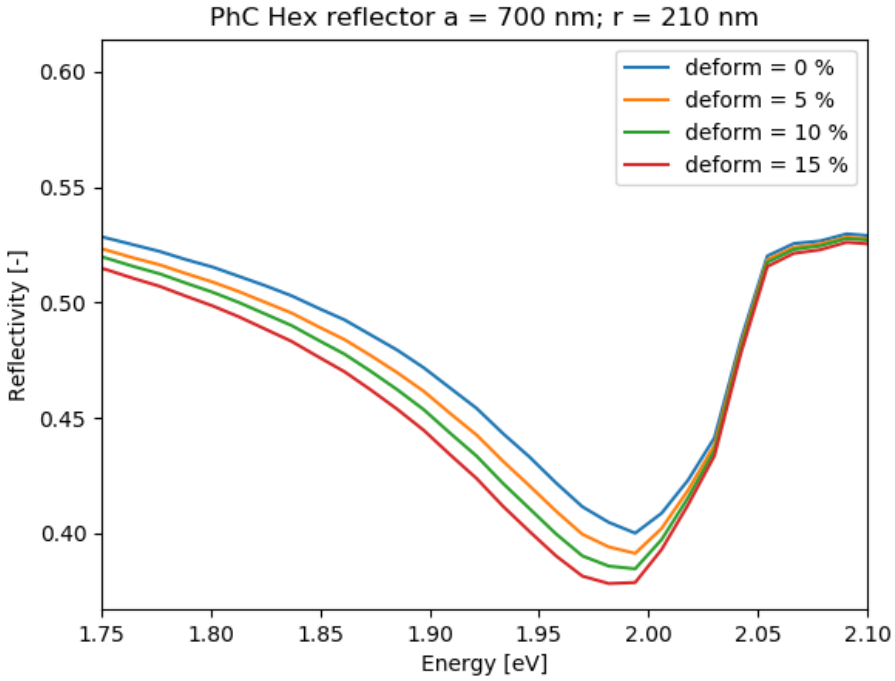

Figure 4.10: The reflectivity of the structure with a hole radius of 210 nm for various values of the deformation parameter. This design corresponds to the geometry with the highest sensitivity, according to the 4.9.

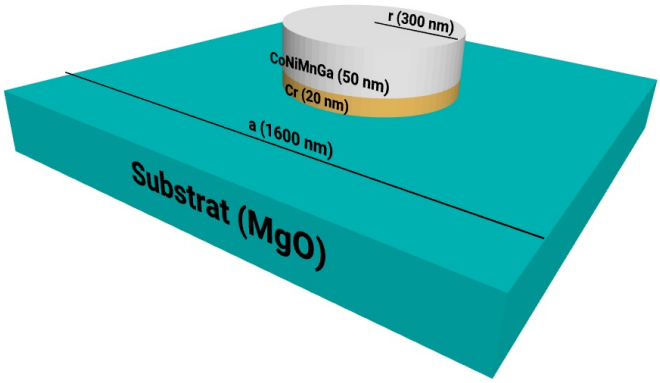

Figure 4.11: An elementary cell of the squere pillar pattern design of the optically active element. This cell is periodically repeated in the simulation.

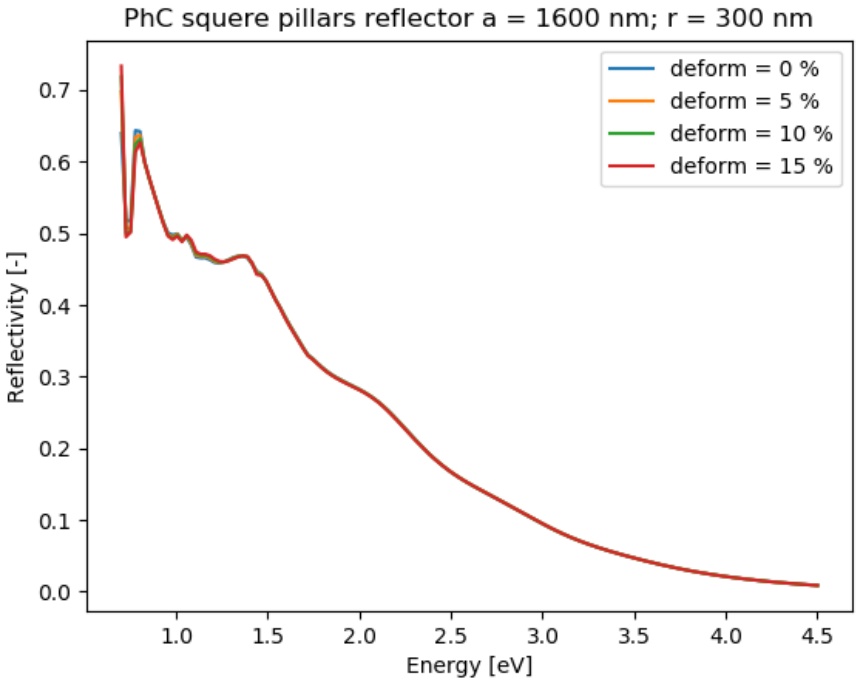

Figure 4.12: Reflectivity of the square lattice pillar structure with a lattice constant 1600 nm. The radius of the pillars is 300 nm. The pillars are made of 50 nm layer of Co:NiMnGa on 20 nm of Cr or 500 nm thick slab of MgO.

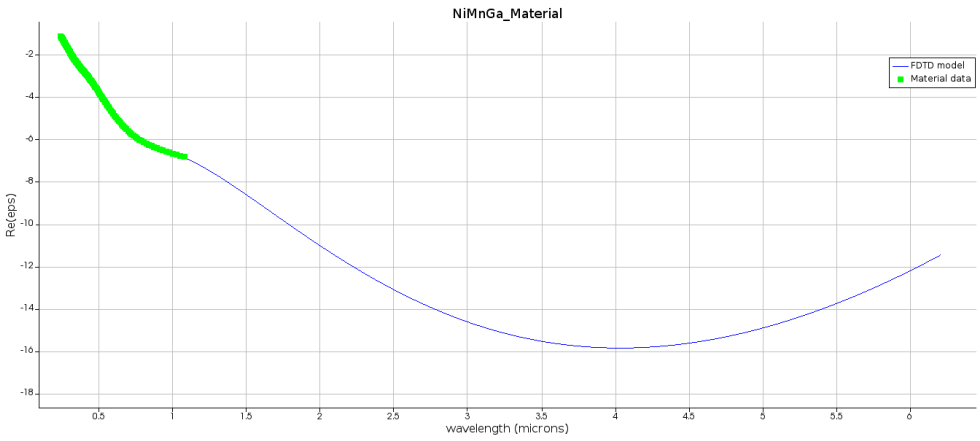

Figure 4.13: A real part of permittivity of Co:NiMnGa material. The spectral region in interest (Fig 4.12) is around 1.5 μm, but valid data ends at 1.1 μm. The figure shows that the fit is unable to provide valid data in the region of interest.

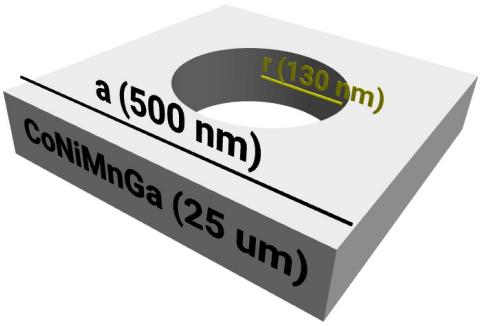

Figure 4.14: An elementary cell of the self-standing foil design of the optically active element. This cell is periodically repeated in the simulation.

4.3 Self-standing film with Squere lattice

We will proceed with variating geometry parameters of the structure to see how does the optical response changes. The structure is a 25 μ thick film of Co:NiMnGa (see figure 4.14) . The lattice constant a and the hole radius r_0 are the variables that we will look at.

The first set of simulations uses parameters $a \in [250, 1500]$ nm and $r_0 \in [50, 0.4 \cdot a_{max}]$ nm The result is displayed in figure 4.15.

The purpose of this figure is only to show how does the structure behaves. Or, more specifically, whether it is possible to shift some spectral features to other energies.

There is clear evidence for spectral features that can be detected. Namely, the drop in reflectivity, which is narrower for lower energies and opens up for higher energies. From this data set, three designs were selected to investigate how do they behave under deformation. The first design has a lattice constant of 900 nm and a hole radius of 210 nm, which produces a narrow drop in reflectivity around 1.25 eV. The second design has a lattice constant of 500 nm and a hole radius of 130 nm, which produces a reflectivity drop in the visible spectrum at around 2 eV. The third design has the reflectivity drop at even higher energies, at around 2.3 eV, but the deformation minima are no longer ordered, and so this design is not suitable for use as a detector. (Fig 4.16)

4.4 optically active element summary

This chapter shows that ferromagnetic shape memory alloys can be used for dynamic control of optical properties. We designed several structures that are sensitive to deformations and change the reflectivity.

The first design is the photonic crystal with cylindrical holes in a hexagonal pattern (figure 4.1) which produces a drop in reflectivity for specific hole radii (figure 4.3). Under various deformation degrees, the reflectivity of the structure changes (figure 4.10). This effect was classified and maximized 4.2.

The second design is a grid of cylindrical pillars in square arrangement (figure

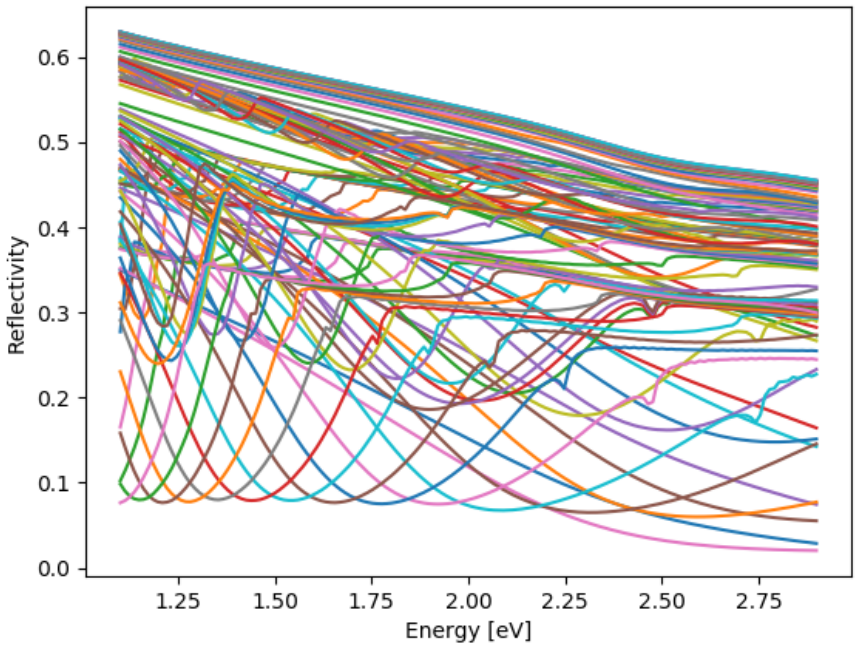

Figure 4.15: The reflectivity of a 25 μm thick film of Co:NiMnGa with cylindrical holes in a squere pattern. The lattice parameter ranges from 250 nm to 1500 nm. The hole radius ranges from 50 nm to 40% of the lattice parameter. Higher curves represent structures with smaller holes, and the radius increases as we go lower in these curves. There is an observable drop in reflectivity which position varies. Structures with a higher value of lattice parameter have a drop in lower energies, while structures with smaller lattice parameter values have a drop in higher energies. The drop in reflectivity opens in higher energies.

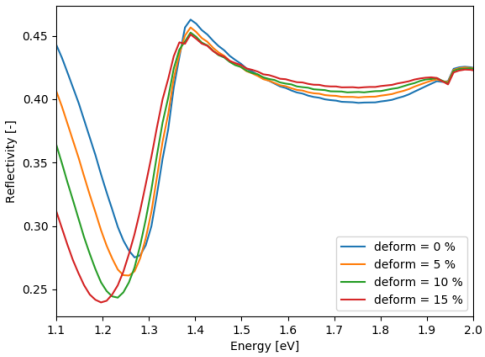

(a) $a = 900$ nm; $r_0 = 210$ nm

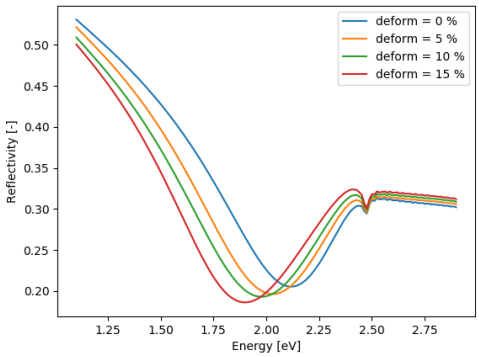

(b) $a = 500$ nm; $r_0 = 130$ nm

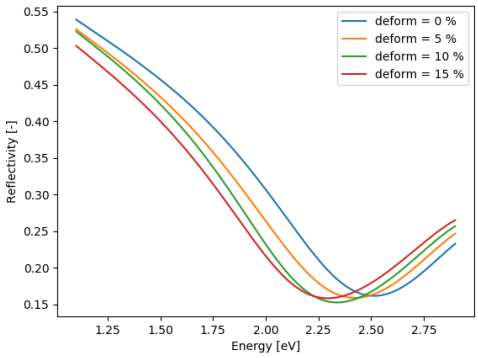

(c) $a = 400$ nm; $r_0 = 110$ nm

Figure 4.16: The reflectivity of 25 μm thick self-standing foil with various hole patterns under different values of deformation.

4.11). This design turned out to be unusable due to the absence of material data for a certain spectral region (figure 4.13). Although, this problem could be solved by modifying the lattice constant of the photonic crystal, this design was abounded. Increasing the lattice constant would be difficult in FDTD simulation.

Due to some worries about integrity, the third design is a self-standing foil with cylindrical holes in a square arrangement. This design turned out to be spectrally flexible (figure 4.15). Three different designs were calculated for the various spectral region (figure 4.16). The question remains whether to detect reflectivity at a specific wavelength or locate the minimum of the reflectivity, but that is up for the application. We believe that self-standing foil is a promissing and suitable design for an application.

Conclusion

The aim of this thesis was to theoretically investigate optical and magneto-optical properties of various metamaterials in form of photonic structures. For this purpose, we have created a custom script that enables us to simulate magneto-optical effects within the FDTD algorithm. The simulation of magneto-optical effect was tested and compared to the result of RCWA and later on a real sample.

Motivated by application in integrated photonic devices, the geometry of multilayered garnet photonic crystal was modified, which led to an emerge of a peak in Faraday rotation, reaching 180° value. It was shown that this resonant peak can be found at various geometries and can be spectrally tuned. The same resonance peak was found using the RCWA method. The Faraday rotation of 45° or higher was found for wavelengths between 438 nm and 472 nm. Replacing a middle layer of the photonic crystal led to an increase of the transmission, leading to an increase of the figure of merit. The figure of merit of such structure is thought to be between 110 and 150, but an investigation of the origin of the resonant behavior of the Faraday rotation revealed that the transmission into zero-diffraction order is much lower. In fact, the figure of merit is only about 20.

An investigation of the origin of the Faraday rotation led to a discovery of strongly located modes of light inside the holes of the photonic crystal. This inspired another potential application, which is a concentration detector. For such device sensitivity of 2.66°/mRIU (refractive index units) was obtained.

Finally, we have simulated three designs of a deformation detector based on memory-shaped alloy - Co:NiMnGa. The first design was a multilayer with cylindrical holes in a hexagonal pattern. The potential shortcoming of this design was that the Co:NiMnGa layer was too thin for the deformation to occur because the substrate under it would not allow the deformation to occur. The second design was a cylindrical pillar pattern, which would solve the deformation problem, but an interesting behavior was found in the spectral region without the support of material data. The third design was a self-standing foil with cylindrical holes in a square pattern. This design showed the highest sensitivity values towards the deformation and simultaneously solved the problem with the non-deforming substrate. The last results opens a way for further development in this field.

Bibliography

[1] Yuya Shoji, Tetsuya Mizumoto, Hideki Yokoi, I-Wei Hsieh, and Richard M Osgood Jr. Magneto-optical isolator with silicon waveguides fabricated by direct bonding. *Applied physics letters*, 92(7):071117, 2008.

[2] Bani Gandhi, Anil Kumar Shukla, and GN Pandey. Design of 1×4 all optical splitter based on 2d photonic crystal. In *Advances in Optical Science and Engineering*, pages 551–557. Springer, 2017.

[3] Hui Wang and Ke-Qin Zhang. Photonic crystal structures with tunable structure color as colorimetric sensors. *Sensors*, 13(4):4192–4213, 2013.

[4] VA Chernenko and S Besseghini. Ferromagnetic shape memory alloys: Scientific and applied aspects. *Sensors and Actuators A: Physical*, 142(2):542–548, 2008.

[5] Miroslav Nyvlt. *Optical interactions in ultrathin magnetic film structures*. PhD thesis, Doctoral thesis, Charles University, 1996.

[6] Polarization ellipse. `https://commons.wikimedia.org/wiki/File:Polarization_ellipse.png`.

[7] PS Pershan. Magneto-optical effects. *Journal of applied physics*, 38(3):1482–1490, 1967.

[8] Ricardo M Silva, Hugo Martins, Ivo Nascimento, José M Baptista, António Lobo Ribeiro, José L Santos, Pedro Jorge, and Orlando Frazão. Optical current sensors for high power systems: a review. *Applied sciences*, 2(3):602–628, 2012.

[9] Verdet constant. `https://www.sciencedirect.com/topics/chemistry/verdet-constant`.

[10] Ondřej Novák. Numerical simulations of optical response of nanostructures using fdtd method. 2019.

[11] Dennis M Sullivan. *Electromagnetic simulation using the FDTD method*. John Wiley & Sons, 2013.

[12] Atef Z Elsherbeni and Veysel Demir. *The finite-difference time-domain method for electromagnetics with MATLAB simulations*. The Institution of Engineering and Technology, 2016.

[13] EE 5303 electromagnetic analysis using finite-difference time-domain. `http://emlab.utep.edu/ee5390fdtd.htm`. Accessed: 2019-03-26.

[14] Faraday effect and optical isolator. `https://support.lumerical.com/hc/en-us/articles/360042274774-Faraday-effect-and-optical-isolator`.

[15] Stefan Visnovsky. *Optics in magnetic multilayers and nanostructures*. Crc Press, 2018.

[16] Patrick Ferrand, M Egen, B Griesebock, Jouni Ahopelto, M Müller, R Zentel, SG Romanov, and CM Sotomayor Torres. Self-assembly of three-dimensional photonic crystals on structured silicon wafers. *Applied Physics Letters*, 81(15):2689–2691, 2002.

[17] Xue Yin Sun, Martin Veis, Jaroslav Kousal, Eva Jesenska, Chen Zhang, Nicolas M Aimon, Taichi Goto, Mehmet C Onbasli, Dong Hun Kim, Hong Kyoon Choi, et al. Srga0. 7co0. 3o3- δ perovskite-cobalt oxide-metal nanocomposite films: magnetic and optical properties. *Nanotechnology*, 26(11):115701, 2015.

[18] Taichi Goto, Mehmet C Onbaşlı, and CA Ross. Magneto-optical properties of cerium substituted yttrium iron garnet films with reduced thermal budget for monolithic photonic integrated circuits. *Optics express*, 20(27):28507–28517, 2012.

[19] P Lázpita, G Rojo, J Gutiérrez, JM Barandiaran, and RC O'Handley. Correlation between magnetization and deformation in a nimnga shape memory alloy polycrystalline ribbon. *Sensor Letters*, 5(1):65–68, 2007.

[20] Valerio Lucarini, Jarkko J Saarinen, Kai-Erik Peiponen, and Erik M Vartiainen. *Kramers-Kronig relations in optical materials research*, volume 110. Springer Science & Business Media, 2005.

List of Figures

List of Abbreviations

FDTD - Finite difference Time domain
FDMA - Ferromagnetic shape memory alloy
MOKE - Magneto-optical Kerr effect
CUDA - Compute Unified Device Architecture
PML - Perfectly matching layer
YIG - Yttrium iron garnet
Ce:YIG - Cerium doped Yttrium iron garnet
Bi:YIG - Bismuth doped Yttrium iron garnet
RCWA - Rigorous coupled wave analysis
FoM - Figure of Merit
RIU - Refractive index unit